Article

Bidirectional perisomatic inhibitory plasticity of a *Fos* neuronal network

https://doi.org/10.1038/s41586-020-3031-0

Received: 28 January 2020

Accepted: 15 October 2020

Published online: 09 December 2020

Check for updates

Ee-Lynn Yap[1], Noah L. Pettit[1], Christopher P. Davis[1], M. Aurel Nagy[1], David A. Harmin[1], Emily Golden[1], Onur Dagliyan[1], Cindy Lin[1], Stephanie Rudolph[1], Nikhil Sharma[1], Eric C. Griffith[1], Christopher D. Harvey[1] & Michael E. Greenberg[1]✉

Behavioural experiences activate the FOS transcription factor in sparse populations of neurons that are critical for encoding and recalling specific events[1–3]. However, there is limited understanding of the mechanisms by which experience drives circuit reorganization to establish a network of *Fos*-activated cells. It is also not known whether FOS is required in this process beyond serving as a marker of recent neural activity and, if so, which of its many gene targets underlie circuit reorganization. Here we demonstrate that when mice engage in spatial exploration of novel environments, perisomatic inhibition of *Fos*-activated hippocampal CA1 pyramidal neurons by parvalbumin-expressing interneurons is enhanced, whereas perisomatic inhibition by cholecystokinin-expressing interneurons is weakened. This bidirectional modulation of inhibition is abolished when the function of the FOS transcription factor complex is disrupted. Single-cell RNA-sequencing, ribosome-associated mRNA profiling and chromatin analyses, combined with electrophysiology, reveal that FOS activates the transcription of *Scg2*, a gene that encodes multiple distinct neuropeptides, to coordinate these changes in inhibition. As parvalbumin- and cholecystokinin-expressing interneurons mediate distinct features of pyramidal cell activity[4–6], the SCG2-dependent reorganization of inhibitory synaptic input might be predicted to affect network function in vivo. Consistent with this prediction, hippocampal gamma rhythms and pyramidal cell coupling to theta phase are significantly altered in the absence of *Scg2*. These findings reveal an instructive role for FOS and SCG2 in establishing a network of *Fos*-activated neurons via the rewiring of local inhibition to form a selectively modulated state. The opposing plasticity mechanisms acting on distinct inhibitory pathways may support the consolidation of memories over time.

Neurons convert new experiences into stable representations in the brain to inform future actions. Mounting evidence suggests that sparse populations of neurons distributed across multiple regions of the brain form the neural substrates for a variety of behaviours[1,2]. A hallmark of these active neuronal ensembles is the transient expression of a set of genes, termed the immediate early genes, one of which encodes the FOS transcription factor[3,7]. It has been a longstanding hypothesis that once activated by salient stimuli, *Fos*-expressing neurons undergo modifications that facilitate the encoding of specific features of an experience, such that subsequent reactivation of even a subset of these neurons is sufficient to elicit recall of the initial experience[1,2]. However, whether these neuronal ensembles become persistently modified, and if so, the nature of these changes and their underlying molecular mechanisms, remain unclear. Moreover, whether *Fos* induction, beyond serving as a proxy for recent neural activity, has a causal role in coordinating circuit modifications required to encode an experience remains unresolved. Complicating progress in this regard is the fact that the Fos family of transcription factors (also known as AP-1) comprises seven at least partially functionally redundant members—FOS, FOSB, FOSL1, FOSL2, JUN, JUNB and JUND[3,7].

Fos-activated neurons in the hippocampal CA1 region have been shown to stably encode contextual information compared with their non-*Fos*-activated counterparts[2]. As recurrent excitatory connectivity is weak within CA1, pyramidal cells (PCs) are known to be regulated in concert either via their common excitatory inputs[8] or through a local network of inhibitory γ-aminobutyric acid-releasing (GABAergic) interneurons (INs). Perisomatic-targeting INs, by virtue of their extensive axonal arborizations, are uniquely positioned to control spike frequency and duration in populations of PCs[4,6]. In this regard, two functionally distinct forms of perisomatic inhibition have been described, mediated by parvalbumin (PV)- or cholecystokinin (CCK)-expressing INs. Whereas PV-INs display fast, non-adapting firing patterns and are predominantly activated in a feedforward fashion, CCK-INs fire regular, adapting trains of spikes and provide predominantly feedback inhibition[4–6,9,10]. Perisomatic inhibition has also been shown to coordinate behavioural state-dependent network oscillations[11,12].

[1]Department of Neurobiology, Harvard Medical School, Boston, MA, USA. ✉e-mail: michael_greenberg@hms.harvard.edu

For example, PV-INs regulate gamma rhythms[12], which are critical for transient synchrony of PCs, and both PV-INs and CCK-INs fire preferentially at different phases of theta rhythms[5], which have been associated with memory encoding or retrieval[13]. By considering how inputs of each IN subtype are selectively modified onto *Fos*-activated neurons, we reasoned that it should be possible to gain mechanistic insights into how experience alters the temporal dynamics of network function to support long-term memories.

Bidirectional modulation of IN inputs

We first tested whether either of these forms of perisomatic inhibition are differentially regulated onto *Fos*-expressing neurons compared to neighbouring non-*Fos*-expressing neurons. We exposed mice to a series of novel environments (NEs), which we observed to activate *Fos* in a sparse subset of CA1 PCs (Fig. 1a, Extended Data Fig. 1a–d). To label these *Fos*-expressing neurons, we used a previously developed adeno-associated virus (AAV)-based reporter that expresses the fluorescent protein mKate2 selectively in recently activated neurons[14] (Fig. 1b). Using this reporter, we detected a significant increase in the number of recently activated (mKate2$^+$) neurons in mice exposed to 2–3 days of NE compared with control mice housed under standard conditions (Fig. 1c). We reasoned that this 2- to 3-day time point would therefore be appropriate for assessing the long-lasting effects of FOS and its late-response target gene(s), which are usually activated within 1–12 h of stimulus onset (Fig. 1d).

To assess PV-mediated inhibition, we expressed channelrhodopsin-2 (ChR2) via a Cre-dependent AAV in PV^{Cre} mice, which express Cre in PV-INs, enabling PV-mediated inhibitory postsynaptic currents (IPSCs) to be selectively evoked by focal photoactivation of ChR2-expressing PV-specific presynaptic boutons. We measured PV-IPSCs in CA1 PCs by performing dual whole-cell voltage-clamp recordings on pairs of recently activated (FOS$^+$mKate2$^+$) and neighbouring non-activated (FOS$^-$mKate2$^-$) PCs in acute hippocampal slices prepared 2–3 days after initial exposure to NEs (Fig. 1e). We found that the mean amplitude of PV-IPSCs in FOS$^+$mKate2$^+$ neurons (311 ± 24 pA (mean ± s.e.m.)) was 1.7-fold larger compared with those in FOS$^-$mKate2$^-$ neurons in either standard or NE conditions (182 ± 12 pA and 181 ± 16 pA, respectively) (Fig. 1f–h), indicating that PV-mediated inhibition is strengthened onto *Fos*-expressing neurons. By contrast, other electrophysiological parameters were not significantly different between the two groups (Extended Data Fig. 1e).

To assess CCK-mediated inhibition, we used an intersectional Flp- and Cre-dependent AAV[15] in Dlx5/6^{Flp};CCK^{Cre} mice to drive the expression of ChR2 specifically in CCK-INs, as the CCK^{Cre} driver alone labels both glutamatergic and GABAergic neurons[16], whereas Dlx5/6^{Flp} causes expression of Flp recombinase only in GABAergic INs (Fig. 1i, Extended Data Fig. 1f, g). Using an analogous experimental paradigm to the one described above, we found that in contrast to the selective increase in PV-mediated inhibition onto *Fos*-activated CA1 PCs, the mean amplitude of CCK-IPSCs in FOS$^+$ CA1 PCs was significantly smaller (166 ± 18 pA, 1.8-fold) compared with that in FOS$^-$ CA1 PCs (293 ± 27 pA) (Fig. 1j–l).

These findings were corroborated by paired recordings of IN-to-CA1 PC to measure amplitudes of unitary IPSCs (uIPSCs). Recordings were performed using slices prepared from PV^{Cre} or Dlx5/6^{Flp}; CCK^{Cre} tdTomato reporter mice 24 h after exposure to kainic acid to synchronously and reliably activate nearly all CA1 PCs (Extended Data Fig. 1c, d). Consistent with our findings using measurements of ChR2-evoked IPSCs, we found that amplitudes of PV-uIPSCs in CA1 PCs were 3.2-fold larger, whereas amplitudes of CCK-uIPSCs in CA1 PCs were 2.2-fold smaller, following exposure to kainic acid (Fig. 1m, Extended Data Fig. 2a–q).

These data indicate that exposure to NEs leads to selective, persistent bidirectional changes in perisomatic inhibition onto *Fos*-expressing neuronal ensembles, with PV-mediated inhibition strengthening,

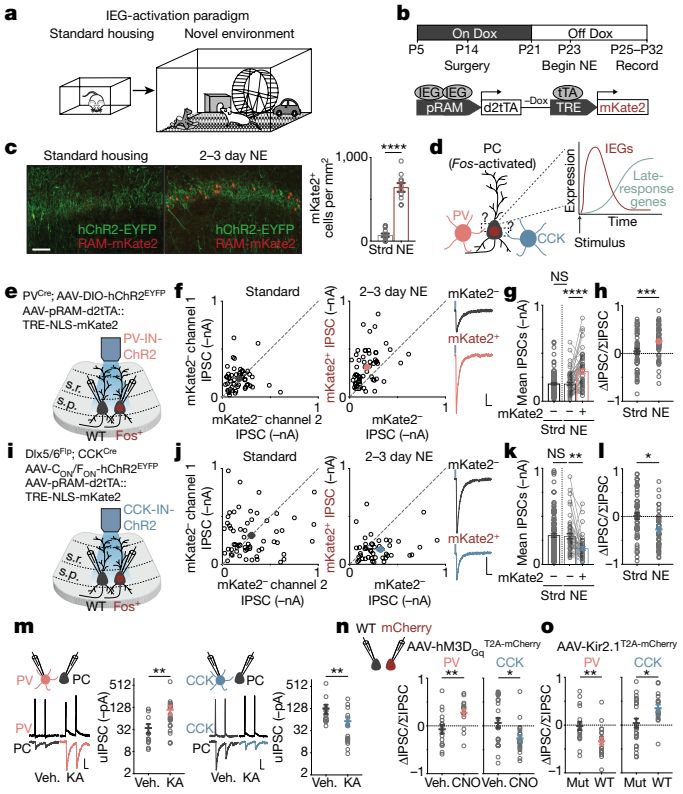

Fig. 1 | Bidirectional perisomatic inhibitory plasticity. a, Schematic of standard (Strd) or NE housing. **b**, Experimental timeline and configuration of the AAV-based activity reporter. Nuclear mKate2 labelling is achieved with a nuclear localization signal (NLS) and temporally controlled with doxycycline (Dox)[14]. IEG, immediate early gene; pRAM, promoter robust activity marking; d2tTA, destabilized tetracycline transactivator; TRE, tTA-responsive element. **c**, Left, representative images depicting *Fos*-activated neurons (red) and PV-IN-specific ChR2 (green) in the hippocampal CA1 region in mice exposed to standard housing or 2–3 days of NE. Right, number of mKate2$^+$ cells per mm^2 in mice exposed to standard (N = 13 mice) and NE conditions (N = 10 mice). Scale bar, 100 µm. ****$P = 2.6 \times 10^{-10}$. **d**, Schematic of a *Fos*-activated CA1 PC and its perisomatic-targeting inputs (indicated with question marks) from PV-INs or CCK-INs. Schematic of activity-induced gene-expression kinetics. In the early wave, immediate early genes such as *Fos* are expressed. FOS subsequently activates late-response genes. **e**, **i**, Schematic of genetic strategy to introduce ChR2 into PV-INs (**e**) or CCK-INs (**i**) and measure light-evoked IPSCs. WT, wild type; s.p., stratum pyramidale; s.r., stratum radiatum. **f**, Scatter plots of recorded pairs of mKate2$^-$ neurons in Strd (left; n = 51/6) or mKate2$^+$ and mKate2$^-$ pairs after 2–3 days of NE (right; n = 58/7) conditions. Representative traces from a pair of neurons shown; blue marks depict light onset. Scale, 100 pA, 40 ms. **g**, Mean PV-IPSC amplitudes from **f**. ****$P = 3.2 \times 10^{-6}$. **h**, Normalized differences in PV-IPSC amplitudes between pairs of neurons in **f** (Methods; Δ indicates the difference in amplitudes between a pair and Σ indicates the sum of the two amplitudes). ***$P = 3.4 \times 10^{-4}$. **j**–**l**, As in **f**–**h**, but for CCK-IPSCs. Strd, n = 60/7; NE, n = 48/8. Scale, 100 pA, 40 ms (**j**). In **k**, **$P = 5.5 \times 10^{-3}$. In **l**, *P = 0.014. **m**, IN-to-CA1 PC paired recording configuration, representative traces and uIPSC amplitudes for PV-IN (left) and CCK-IN (right) to CA1 PC pairs. Veh., vehicle; KA, kainic acid. PV-IN to CA1 PC: vehicle, n = 13/6; KA, n = 19/7; **P = 0.003. CCK-IN to CA1 PC: vehicle: n = 16/9; KA, n = 16/4; **$P = 9.6 \times 10^{-3}$. Scale, 30 mV (IN response), 20 pA (PC response), 20 ms. Two-sided Mann–Whitney test. **n**, Normalized differences in amplitudes of PV-IPSCs (left) and CCK-IPSCs (right) of pairs of untransduced (WT) and hM3D$_{Gq}$ (mCherry$^+$) neurons 24 h after treatment with vehicle or clozapine *N*-oxide (CNO). PV (vehicle, n = 16/5; CNO, n = 16/7; **P = 0.006); CCK (vehicle, n = 22/5; CNO, n = 21/7; *P = 0.014). **o**, As in **n** but with Kir2.1. The control is a non-conducting mutant (KirMut). Mice were exposed to NEs for 7–10 days, a period over which many CA1 PCs would have expressed *Fos* (Extended Data Fig. 1c, d). PV (KirMut, n = 18/3; Kir2.1, n = 19/5; **P = 0.007); CCK (KirMut, n = 25/3; Kir2.1, n = 17/4; *P = 0.023). In **f**, **h**, **j**, **l**, **m**–**o**, each open circle represents a pair of simultaneously recorded neurons. In **f**, **j**, **m**–**o**, n is expressed as number of pairs/number of mice. Data are mean ± s.e.m. (**c**, **f**–**h**, **j**–**o**); two-sided t-test (**c**, **h**, **l**, **n**, **o**); ordinary one-way ANOVA, corrected for multiple comparisons (**g**, **k**).

and CCK-mediated inhibition weakening. Hereafter, we refer to these modifications as 'bidirectional perisomatic inhibitory plasticity'.

The bidirectional changes in perisomatic inhibition are a consequence of experience-driven neuronal activity, rather than a reflection of pre-existing differences between $FOS^{+}mKate2^{+}$ and $FOS^{-}mKate2^{-}$ CA1 PCs, insofar as they could be recapitulated by chemogenetic activation of neurons expressing the G_q-coupled DREADD[17] receptor $hM3D_{Gq}$ (Fig. 1n, Extended Data Fig. 3a–e). Conversely, silencing CA1 PCs by expression of an inwardly rectifying potassium channel Kir2.1[18], but not a non-conducting mutant (KirMut), had the opposite effect (Fig. 1o, Extended Data Fig. 3f, g).

Causal role of Fos family transcription factors

Since the induction of bidirectional perisomatic inhibitory plasticity occurs selectively on *Fos*-expressing CA1 PCs, we considered the possibility that the Fos family of transcription factors might mediate these changes. We first determined which of the seven family members are induced in the hippocampus by neuronal activity (Fig. 2a). We found that *Fos*, *Fosb* and *Junb* were induced by approximately 100-fold or more in membrane-depolarized hippocampal cultured neurons, whereas the other four Fos family members were significantly less responsive (Fig. 2b). We therefore developed a triple-conditional-knockout mouse line (*Fos*$^{fl/fl}$;*Fosb*$^{fl/fl}$;*Junb*$^{fl/fl}$, hereafter FFJ)[19] to enable the deletion of these strongly inducible AP-1 factors in a spatiotemporally controlled manner, and verified the effective excision of these genes upon Cre expression in vivo by single-molecule RNA fluorescence in situ hybridization (smRNA-FISH) and immunostaining for each of the three proteins (Extended Data Fig. 4a-f).

Following sparse deletion of *Fos*, *Fosb* and *Junb* mediated by AAV expressing Cre (Fig. 2c, d), we performed dual whole-cell recordings from FFJ-wild-type (FFJ-WT) and neighbouring FFJ-knockout (FFJ-KO) CA1 PCs while electrically stimulating perisomatic inhibitory axons. We found a 1.7-fold decrease in pharmacologically isolated evoked IPSC (eIPSC) amplitudes in FFJ-KO compared with FFJ-WT activated neurons (Fig. 2e, Extended Data Fig. 4g–i). By contrast, we observed no significant differences in amplitudes of CA3 Schaffer collateral-evoked excitatory postsynaptic currents (eEPSCs) or proximal dendritic eIPSCs between FFJ-WT and FFJ-KO neurons 24 h after treatment with vehicle or kainic acid (Fig. 2f, g, Extended Data Fig. 4j–o). Therefore, although AP-1 could, in principle, regulate *Fos*-activated CA1 PCs by modulating their CA3 excitatory inputs or inhibition from distinct compartments, AP-1 factors are specifically required for the regulation of perisomatic inhibition.

To directly measure PV-mediated inhibition, we generated $PV^{Flp/Flp}$;FFJ mice, which enabled the expression of ChR2 specifically in PV-INs (Fig. 2h). Simultaneous slice recordings of ChR2-evoked PV-IPSCs in FFJ-WT and neighbouring FFJ-KO neurons revealed no differences in standard-housed mice (Fig. 2i). By contrast, there was a significant decrease in amplitudes of PV-IPSCs in FFJ-KO cells in mice after 7–10 days of NE, with 90% of FFJ-KO cells showing smaller IPSC amplitudes compared with the average for FFJ-WT cells (Fig. 2i, j). These data indicate that AP-1 factors are required for the experience-dependent recruitment of PV-mediated inhibition and identify a previously elusive role for AP-1 factors in long-term plasticity.

Given that loss of AP-1 leads to defects in inhibition, we next tested whether spatial learning and memory are affected under these conditions[20]. FFJ mice were bilaterally injected with AAV expressing Cre (FFJ-KO) or a catalytically inactive ΔCre (FFJ-WT) in the CA1 region and assessed in the Morris water maze paradigm. FFJ-KO mice performed significantly worse on this spatial task than the FFJ-WT mice, and were unable to learn the location of the platform in the maze (Fig. 2k, l). We observed no significant differences in mean swim speeds or path lengths between the two groups, arguing against a contribution of motor deficits in the FFJ-KO mice (Fig. 2m). These results suggest that changes in perisomatic inhibitory plasticity of *Fos*-activated neuronal networks may contribute to hippocampus-dependent spatial learning.

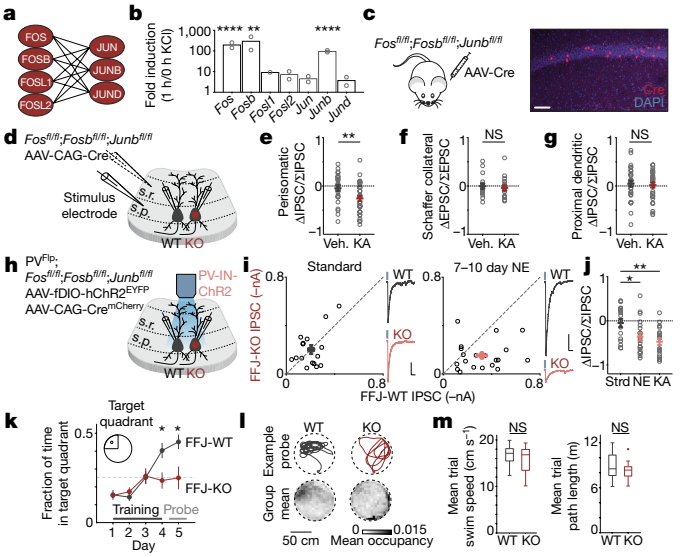

Fig. 2 | Causal role of Fos family transcription factors. a, Schematic depicting possible AP-1 dimerization. **b**, Mean fold induction of each AP-1 member upon KCl-mediated depolarization in hippocampal neurons (bulk RNA-sequencing), showing significantly more induction of *Fos* (****$P = 9.1 \times 10^{-5}$), *Fosb* (**$P = 0.008$) and *Junb* (****$P = 2.2 \times 10^{-7}$) compared to the four other factors. $n = 2$ biological replicates. **c**, FFJ mice were transduced with AAV to sparsely express Cre (red). Representative CA1 image shown. Scale bar, 100 µm. **d**, Recording configuration with stimulus electrode placement in stratum pyramidale, to measure perisomatic eIPSCs, or stratum radiatum, for Schaffer collateral eEPSCs or proximal dendritic eIPSCs. **e**–**g**, Normalized differences in indicated pharmacologically isolated current amplitudes between pairs of FFJ-WT and FFJ-KO PCs: perisomatic eIPSCs (**e**), Schaffer collateral eEPSCs (**f**) and proximal dendritic eIPSCs (**g**). **e**, Vehicle, $n = 26/6$; KA, $n = 33/7$; **$P = 0.005$. **f**, Vehicle, $n = 18/5$; KA, $n = 17/4$. **g**, Vehicle, $n = 30/4$; KA, $n = 30/6$. **h**, Schematic of strategy to introduce ChR2 in PV-INs and sparse Cre into the CA1 of PV^{Flp};FFJ mice. **i**, Scatter plots of recorded pairs of FFJ-WT and FFJ-KO CA1 PCs in mice in standard (left; $n = 16/3$) or 7–10 day NE (right; $n = 20/3$) conditions. Representative traces from pairs of neurons shown; blue marks depict light onset. Scale, 50 pA (left) or 100 pA (right), 40 ms. **j**, As in **e**–**g** for pairs depicted in **i** and 24 h after kainic acid treatment ($n = 19/3$). *$P = 0.014$ (NE), **$P = 0.002$ (KA). Ordinary one-way ANOVA, corrected for multiple comparisons. **k**, Fraction of time spent swimming in target quadrant for FFJ-WT ($N = 11$) and FFJ-KO ($N = 12$) mice. *$P = 0.014$ (day 4); 0.016 (day 5), where day 1 is defined as the start of training. **l**, Top, example probe trial swim traces. Bottom, mean probe trial occupancy maps (5-cm bins). **m**, Box plots of mean trial swim speed (left) and path length (right); mice as in **k**. In box plots, the centre line shows median, box edges indicate top and bottom quartiles, whiskers extend to minimum and maximum values and + indicates an outlier. In **e**–**g**, **i**, **j**, each open circle represents a pair of simultaneously recorded neurons; n is expressed as number of pairs/number of mice. Data are mean ± s.e.m. (**e**–**g**, **i**–**k**); two-sided t-test (**b**, **e**–**g**, **k**, **m**).

FOS targets in CA1 pyramidal neurons

Although many activity-regulated genes (ARGs) have now been defined, difficulties in effectively disrupting AP-1 function in vivo have complicated the identification of genes that are specifically regulated by AP-1 factors and thus might mediate the bidirectional modulation of perisomatic inhibition. The identification of AP-1 target genes has been further hampered by the pronounced neuronal cell-type-divergence of activity-dependent gene programs[21], and it is unclear how AP-1 factors, which are induced in nearly all cell types in the brain, contribute to this diversity. To address these challenges, we used a suite of genome-wide approaches to identify high-confidence AP-1 targets, focusing on CA1 PCs. We identified (1) ARGs in CA1 PCs; (2) genes that show reduced

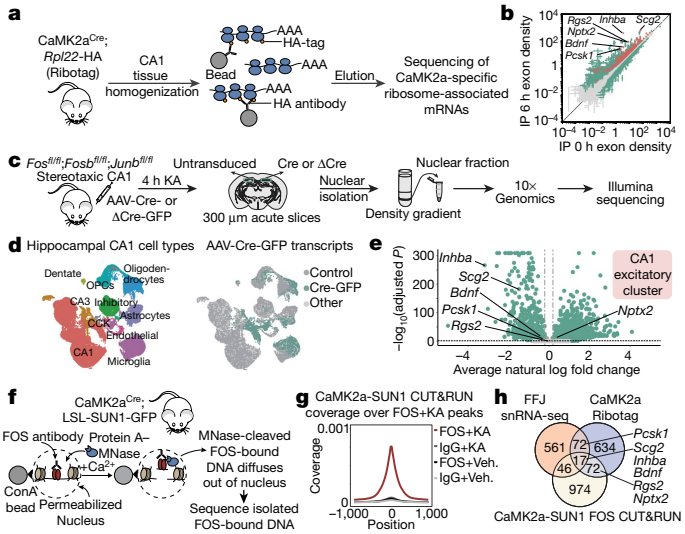

Fig. 3 | FOS targets in CA1 pyramidal neurons. a, **c**, **f**, Workflow for Ribotag (**a**), FFJ snRNA-seq (**c**) and FOS CUT&RUN (**f**). **b**, Scatter plot showing CaMK2a-specific ARGs 6 h after kainic acid treatment compared with vehicle. Significantly different genes are indicated in green; FDR ≤ 0.005. CaMK2a-enriched (immunoprecipitated (IP) over input) genes are additionally indicated in red. Points represent mean ± s.e.m. $n = 4$ mice per biological replicate; 3 biological replicates per condition. **d**, UMAP visualization of nuclei from Cre$^+$ and control FFJ snRNA-seq with cell-type information (left) or genotype assignments (right) overlaid. Control, Cre$^-$ cells in untransduced hemispheres; Cre-GFP, Cre$^+$ cells in injected hemispheres; other, Cre$^-$ cells in injected hemispheres or Cre$^+$ cells in untransduced hemispheres. $n = 58{,}536$ cells, 6 mice. **e**, Volcano plot of genes in the CA1 excitatory cluster. *y*-axis shows $-\log_{10}$ Bonferroni-corrected *P*-values (two-sided Wilcoxon rank-sum test). Fold changes are calculated from Cre$^+$ compared with control cells. Each point represents a gene detected in at least 5% of untransduced cells. Light grey, $P \geq 0.05$ ($n = 3{,}429$); dark grey, fold change < 20% in either direction ($n = 42$); green, $P < 0.05$ and fold change ≥ 20% ($n = 3{,}514$). **g**, Aggregate plot showing spike-in normalized FOS coverage per bin averaged across all FOS peaks for CaMK2a–SUN1 CUT&RUN. IgG serves as a specificity control. $n = 1$ mouse per biological replicate, 3 biological replicates per condition. **h**, Venn diagram showing the intersection of significant CA1 PC-specific genes from CaMK2a–Ribotag (fold change ≥ 2), FFJ snRNA-seq (≥ 20% decreased expression in FFJ-KO cells) and CUT&RUN (FOS peaks within 10 kb of the TSS). Schematic image in **c** (middle) adapted with permission from Paxinos & Franklin (ref. [32]).

expression when AP-1 function is disrupted; and (3) genes that display activity-dependent FOS binding at nearby regulatory DNA elements. For these analyses, we treated mice with kainic acid to strongly activate nearly all cells in CA1 and thus maximize the signal-to-noise ratio for gene identification. AP-1 target(s) of interest identified by this method were subsequently validated under the more physiological condition of NE exposure.

We first defined ARGs specific to CA1 PCs by profiling cell-type-specific ribosome-associated mRNAs (Fig. 3a). Using CA1 tissue from CaMK2a^{Cre};*Rpl22*-HA (Ribotag)[22] mice treated with 6 h vehicle or kainic acid, we immunoprecipitated and sequenced CaMK2a-specific ribosome-associated mRNAs. Analysis of differentially expressed genes identified 795 ARGs induced by at least twofold (false discovery rate (FDR) ≤ 0.005), of which 111 were significantly enriched in CaMK2a-positive neurons relative to other cell types, including PV-INs (Fig. 3b, Extended Data Fig. 5a).

To determine which of these genes show reduced expression when AP-1 function is disrupted, we performed high-throughput single-nucleus RNA-sequencing (snRNA-seq) using the FFJ mice. The mice were injected with AAV expressing Cre–GFP or ΔCre–GFP into one CA1 hemisphere, leaving cells in the contralateral hemisphere as untransduced controls. Mice were treated with kainic acid, and 4 h later CA1 nuclei were isolated and subsequently sorted using the 10X Genomics platform (Fig. 3c). We sequenced 83,750 single-cell transcriptomes isolated from 6 Cre$^+$ and 4 ΔCre$^+$ mice (Fig. 3d, Extended Data Fig. 5b–e). Nuclei were clustered into 12–15 cell types using the Seurat single-cell analysis pipeline (Fig. 3d). The presence of viral-derived transcripts was used to identify 17,027 Cre$^+$ and 14,557 ΔCre$^+$ nuclei. For each cell type, differential gene-expression analysis comparing Cre$^+$ (or ΔCre$^+$) nuclei to their respective untransduced controls was used to identify AP-1-regulated genes, many of which are cell-type-specific (Extended Data Fig. 5f, g). These data support the longstanding but previously untested hypothesis that AP-1 contributes to the cell-type divergence of ARG expression. Specifically, within the CA1 excitatory neuron cluster, we identified 696 genes that were significantly downregulated by at least 20% in the absence of AP-1 (Fig. 3e, Extended Data Fig. 5e–h).

Finally, we identified genes that are probable direct targets of FOS in CA1 PCs using CUT&RUN, a chromatin-profiling strategy in which in situ antibody-targeted controlled cleavage by micrococcal nuclease releases specific FOS–DNA complexes for sequencing[23] (Fig. 3f). CaMK2a-expressing CA1 nuclei from CaMK2a^{Cre};LSL-Sun1-sfGFP-Myc[24] mice were isolated by sorting on the basis of Cre-dependent expression of the GFP-tagged inner nuclear membrane protein SUN1. We identified 3,295 FOS-bound activity-responsive loci from mice exposed to kainic acid for 2–3 h compared with vehicle treatment, with 1,109 genes containing at least one FOS-bound regulatory element within 10 kb of the transcription start site (TSS) (Fig. 3g, Extended Data Fig. 6a–f, Supplementary Fig. 1).

Intersection of the three datasets identified 17 genes that were inducible by activity in CA1 PCs (CaMK2a–Ribotag), showed reduced expression with loss of AP-1 (FFJ snRNA-seq) and bound FOS at nearby regulatory elements (CaMK2a–SUN1 FOS CUT&RUN). An additional 190 genes were present in two of the three datasets (Fig. 3h, Supplementary Table 1). We focused our attention on three high-confidence AP-1-regulated candidate genes that displayed high fold induction and whose expression was enriched in CA1 PCs (*Inhba*, *Bdnf* and *Scg2*) and three other genes that were previously shown to contribute to inhibitory plasticity[25] and were present in two of the three genomic datasets (*Rgs2*, *Nptx2* and *Pcsk1*) (Extended Data Figs. 6g–k, 7a).

FOS-dependent effector of inhibition

To identify molecular effector(s) of bidirectional perisomatic inhibitory plasticity downstream of FOS activation, short hairpin RNA (shRNA)-mediated gene knockdown was initially used to determine whether any of the six candidate genes might mediate the activity-dependent strengthening of PV-mediated inhibition. After verifying the efficiency of knockdown in neurons (Extended Data Fig. 7b) and the absence of adverse effects on overall neuronal viability, individual shRNAs were cloned into a Flp-OFF AAV, enabling payload inactivation by Flp recombinase and the exclusion of shRNA expression in GABAergic INs when using Dlx5/6^{Flp} mice (Fig. 4a, b, Extended Data Fig. 7c, Supplementary Fig. 2a).

Following sparse transduction of neurons, we simultaneously measured PV-IPSCs in neighbouring pairs of shRNA-positive (mCherry$^+$) and -negative (mCherry$^-$) PCs by photostimulating PV-specific ChR2-expressing boutons in Dlx5/6^{Flp};PV^{Cre} mice that had been treated with kainic acid 24 h earlier (Fig. 4b). We found no effects on amplitudes of PV-IPSCs upon expression of a control shRNA or shRNAs against *Inhba*, *Rgs2*, *Nptx2* or *Pcsk1*, and only a slight decrease with knockdown of *Bdnf*[26] (Fig. 4c, Extended Data Fig. 7d). By contrast, PV-mediated inhibition was significantly decreased by either of two independent shRNAs against *Scg2* (Fig. 4c, d, Extended Data Fig. 7e). Similar results were observed following the more physiological condition of NE exposure

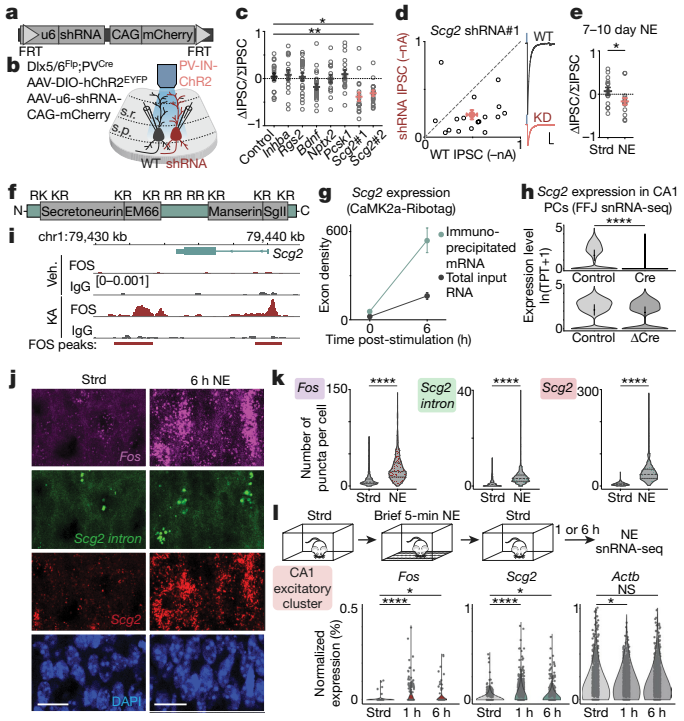

Fig. 4 | FOS-dependent effector of inhibition. a, **b**, Schematic of Flp-OFF shRNA AAV construct (**a**) and recording strategy used (**b**). CAG, CAG promoter; FRT, FRT cassette; U6, U6 promoter. **c**, Normalized differences in PV-IPSC amplitudes between pairs of shRNA$^-$ and shRNA$^+$ PCs 24 h after kainic acid treatment. Control, $n = 17/9$; *Inhba*, $n = 15/4$; *Rgs2*, $n = 20/3$; *Bdnf*, $n = 26/10$; *Nptx2*, $n = 16/3$; *Pcsk1*, $n = 17/6$; *Scg2*#1, $n = 17/7$ (**$P = 0.002$); *Scg2*#2, $n = 17/6$ (*$P = 0.016$). Ordinary one-way ANOVA, with multiple comparisons correction. **d**, Scatter plot of recorded PV-IPSC amplitudes for *Scg2*#1 shRNA shown in **c**. Representative traces from a pair of neurons shown; blue marks depict light onset. $n = 17/7$. Scale, 100 pA, 40 ms. **e**, As in **c**, for *Scg2*#1 shRNA in standard ($n = 14/5$) or 7–10 day NE ($n = 16/4$) conditions. *$P = 0.048$. **f**, Schematic of SCG2 protein, depicting the four SCG2-derived neuropeptides and nine dibasic (KR, RK or RR) cleavage residues. **g**, *Scg2* expression from CaMK2a–Ribotag (Fig. 3b), showing induction and enrichment (IP over input) 6 h after kainic acid treatment. **h**, Violin plots depicting *Scg2* expression in CA1 PCs in Cre or ΔCre compared with the respective controls from FFJ snRNA-seq (Fig. 3e). TPT, tags per ten thousand reads. ****$P = 2.9 \times 10^{-182}$ and ≥ 20% decrease. Data are mean ± 2 × s.d. **i**, Tracks displaying FOS-binding sites surrounding the *Scg2* locus from CUT&RUN (Fig. 3g). The *y*-axis shows spike-in normalized coverage scaled to maximum value (in brackets) observed at the displayed locus. **j**, Representative smRNA-FISH images of CA1 in mice exposed to standard and 6 h NE conditions, probing for *Fos* (magenta), mature *Scg2* (red) and intron-targeting *Scg2* (green) transcripts (lower magnification shown in Extended Data Fig. 7h). Strd, $N = 4$; NE, $N = 6$ mice. Scale, 20 µm. **k**, Violin plots showing number of puncta per cell for smRNA-FISH in **j**. Dashed lines indicate medians and quartiles, each point represents a cell. Strd, $n = 909$; NE, $n = 1{,}548$ cells. ****$P < 1 \times 10^{-15}$. **l**, Top, workflow of NE snRNA-seq. Mice were exposed to NE briefly (5 min) and returned to standard housing for 1 h or 6 h before CA1 dissection. Bottom, violin plots of normalized gene expression in CA1 PCs ($n = 1{,}659$ cells after downsampling). Strd, $N = 2$ mice; NE (1 h and 6 h), $N = 4$ mice each. *Fos*: ****$P = 4.2 \times 10^{-9}$, *$P = 0.025$; *Scg2*: ****$P = 2.2 \times 10^{-16}$, *$P = 0.032$; *Actb*: *$P = 0.014$. In **c**–**e**, each open circle represents a pair of simultaneously recorded neurons, *n* is expressed as number of pairs/number of mice. Data are mean ± s.e.m. (**c**–**e**, **g**); two-sided *t*-test (**e**, **k**); two-sided Wilcoxon rank-sum test (**h**, **l**).

(Fig. 4e, Extended Data Fig. 7f), suggesting a prominent role for CA1 PC-derived *Scg2* in the long-term regulation of PV-mediated inhibition.

Scg2 has previously been shown to be activity-regulated[27] and to encode a neuropeptide precursor that undergoes endoproteolytic processing by PCSK1/2 proteases[28] to produce four distinct, non-overlapping neuropeptides: secretoneurin, EM66, manserin and

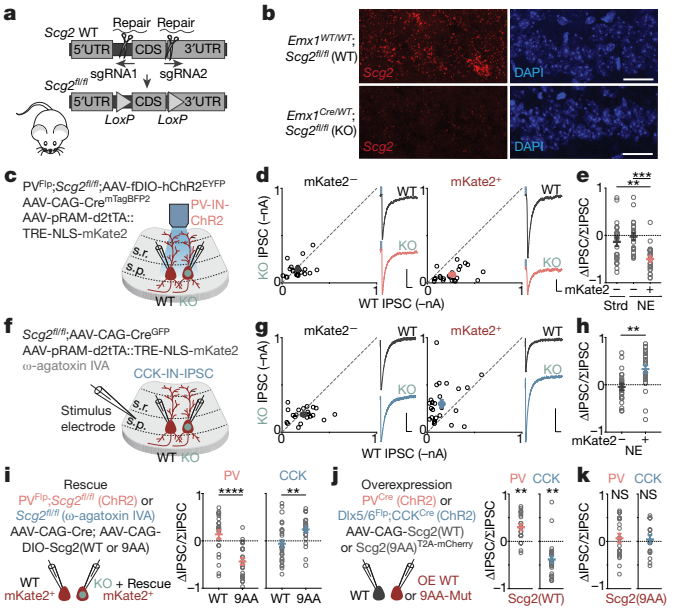

Fig. 5 | *Scg2* mediates bidirectional perisomatic inhibitory plasticity. **a**, Schematic depicting strategy for generation of a *Scg2*$^{fl/fl}$ mouse line using CRISPR–Cas9. CDS, coding sequence; UTR, untranslated region. **b**, smRNA-FISH validation of *Scg2*$^{fl/fl}$ crossed to *Emx1*^{Cre} to excise *Scg2* in all excitatory cells. $N = 2$ mice per line. Scale bar, 20 µm. **c**, Schematic of strategy to introduce ChR2 in PV-INs in PV^{Flp};*Scg2*$^{fl/fl}$ mice, mark recently active cells with the viral mKate2 activity reporter and sparsely transduce Cre into CA1 PCs. **d**, Scatter plots of recorded mKate2$^-$ (left; $n = 21/4$) or mKate2$^+$ (right; $n = 22/9$) pairs of *Scg2*-WT and *Scg2*-KO neurons after 2–3 day NE exposure. Representative traces from pairs of neurons shown; blue marks depict light onset. Scale, 50 pA, 40 ms. **e**, Normalized differences in PV-IPSC amplitudes between pairs of neurons in **d** and mKate2$^-$ pairs from standard housing ($n = 22/5$). **$P = 0.004$, ***$P = 1.4 \times 10^{-4}$. Ordinary one-way ANOVA, with multiple comparisons correction. **f**, Schematic of pharmacological strategy used to isolate CCK-IPSCs in *Scg2*$^{fl/fl}$ mice. NBQX, (*R*)-CPP (*N*-methyl-D-aspartate antagonist) and ω-agatoxin IVA (to block PV-IPSCs) were used. **g**, **h**, As in **d**, **e**, but for CCK-IPSCs. mKate2$^-$, $n = 22/6$; mKate2$^+$, $n = 26/6$. Scale, 100 pA, 40 ms. **$P = 0.001$. **i**–**k**, As in **e**, **h**, for pairs of neurons depicted in **i**, **j**. **i**, PV: WT, $n = 22/5$; 9AA, $n = 23/4$, ****$P = 1.2 \times 10^{-5}$; CCK: WT, $n = 27/3$; 9AA, $n = 23/4$, **$P = 0.005$. **j**, PV: $n = 20/5$, **$P = 0.001$; CCK: $n = 25/3$, **$P = 0.004$. **k**, PV: $n = 19/4$; CCK: $n = 16/3$. In **d**, **e**, **g**–**k**, each open circle represents a pair of simultaneously recorded neurons; data are mean ± s.e.m.; *n* = number of pairs/number of mice. Two-sided *t*-test (**h**, **i**); two-sided one-sample *t*-test with hypothetical mean of 0 (**j**, **k**).

SgII (Fig. 4f); however, the functions of these peptides in the brain are largely unknown. We found that *Scg2* is highly enriched in CA1 PCs (Fig. 4g), significantly downregulated upon AP-1 loss (Fig. 4h), and associated with several FOS-bound regulatory elements (Fig. 4i).

To test whether *Scg2* is expressed in the CA1 region in an experience-dependent manner, we performed smRNA-FISH using mice exposed to 6 h NE compared to standard-housed mice, probing for mature *Fos* and *Scg2* RNA, as well as nascent intron-containing *Scg2* transcripts (Fig. 4j). *Fos* and *Scg2* showed correlated expression (Extended Data Fig. 7g, h), with both genes significantly induced following NE exposure (Fig. 4k). We also found that a brief (5-min) NE exposure was sufficient to induce *Fos* and *Scg2* in CA1 PCs when assessed by snRNA-seq 1 h or 6 h after the exposure (Fig. 4l).

Scg2 regulates PV and CCK inhibition

To investigate further the requirement of *Scg2* for bidirectional perisomatic inhibitory plasticity, we generated and verified an *Scg2* conditional-knockout mouse line (*Scg2*$^{fl/fl}$; Fig. 5a, b, Extended Data Fig. 8a). We crossed these with PV^{Flp} mice. The resulting PV$^{Flp/Flp}$;*Scg2*$^{fl/fl}$

mice were sparsely transduced with AAV expressing Cre, co-injected with the AAV mKate2 activity reporter (Fig. 1b) and a separate Flp-dependent AAV to localize ChR2 expression to PV-INs (Fig. 5c). We then exposed these mice to 2–3 days of NE and subsequently recorded light-evoked PV-IPSCs simultaneously in neighbouring *Fos*-activated neurons that were positive (*Scg2*-KO $Cre^{+}mKate2^{+}$) or negative (*Scg2*-WT $Cre^{-}mKate2^{+}$) for Cre (Fig. 5c). Consistent with the data obtained by shRNA-mediated knockdown of *Scg2*, we found that amplitudes of PV-IPSCs in *Fos*-activated *Scg2*-KO neurons were on average threefold smaller compared with those in *Scg2*-WT neurons (Fig. 5d, e). This effect was not observed in non-*Fos*-activated ($mKate2^{-}$) neurons in either standard or NE conditions (Fig. 5d, e). Thus, *Fos*-activated CA1 PCs require *Scg2* to induce plasticity of PV-IN synapses.

We next investigated whether *Scg2* also regulates CCK-mediated inhibition. Owing to the lack of a CCK-IN-only Flp-driver line, we used two orthogonal approaches to measure CCK-IPSCs. First, we used a pharmacological strategy in which CCK-IPSCs were specifically measured by blocking PV-IPSCs with ω-agatoxin IVA[4,10]. Simultaneous recordings from pairs of *Scg2*-WT ($Cre^{-}mKate2^{+}$) and *Scg2*-KO ($Cre^{+}mKate2^{+}$) neurons after 2–3 days of NE exposure showed that the mean amplitude of CCK-IPSCs in *Scg2*-KO neurons was twofold larger than that in *Scg2*-WT neurons specifically upon *Fos* activation (Fig. 5f–h). Similar results were obtained with an independent approach involving our intersectional genetic strategy, using $Dlx5/6^{Flp}$; CCK^{Cre} mice in conjunction with shRNA-mediated knockdown of *Scg2* (Extended Data Fig. 8b–f). Thus, a single experience-regulated AP-1 target, *Scg2*, couples the bidirectional regulation of PV- and CCK-mediated inhibition onto *Fos*-activated neurons.

These findings were further corroborated through a series of rescue and overexpression experiments. Notably, we found that the defects in both PV- and CCK-mediated inhibition were restored to control levels when *Scg2* was exogenously expressed in shRNA-mediated knockdown or $Scg2^{fl/fl}$ knockout experiments (Fig. 5i, Extended Data Figs. 8g, 9a–d). In addition, we compared amplitudes of light-evoked PV- or CCK-IPSCs in *Scg2*-overexpressing (*Scg2*-OE) and neighbouring control (*Scg2*-WT) neurons, and found that gain-of-function of SCG2 was sufficient to strengthen PV- and weaken CCK-mediated inhibition, respectively, in the absence of neural activity (Fig. 5j, Extended Data Fig. 9e, f).

Cleavage of the SCG2 precursor is known to give rise to multiple neuropeptides with potentially distinct functions (Fig. 4f). Given that SCG2 cleavage is directed by a series of internal dibasic residues, we generated a cleavage-resistant form of SCG2 in which the nine dibasic sequences were mutated to alanine (9AA-Mut). Having first verified that these sequence changes do not affect SCG2 expression levels (Extended Data Fig. 9g, Supplementary Fig. 2b), we found that expression of this cleavage-deficient SCG2 did not recapitulate the effects of overexpressing wild-type SCG2 (Fig. 5k, Extended Data Fig. 9h, i) or rescue the effects of loss of *Scg2* (Fig. 5i, Extended Data Fig. 9c, d). Thus, while we cannot formally exclude other modes of SCG2 action, such as the contribution to dense-core-vesicle biogenesis or the packaging of neuropeptides into dense-core vesicles[28], our results suggest that the processing of SCG2 precursor protein to mature peptides may be required for experience-dependent bidirectional perisomatic inhibitory plasticity, raising the possibility that distinct SCG2-derived peptides might coordinate aspects of bidirectional plasticity.

Scg2 is critical for network rhythms in vivo

To determine whether the FOS–SCG2 pathway alters the function of hippocampal networks in vivo, we assessed the effects of disrupting *Scg2* function on hippocampal network oscillations. We performed silicon probe recordings in awake head-fixed mice running on an air-supported ball (Fig. 6a). $Scg2^{fl/fl}$ mice were injected with AAV expressing ΔCre (*Scg2*-WT) or Cre (*Scg2*-KO) bilaterally into the CA1 (Extended Data Fig. 10a). We found that the frequency spectra in the gamma range

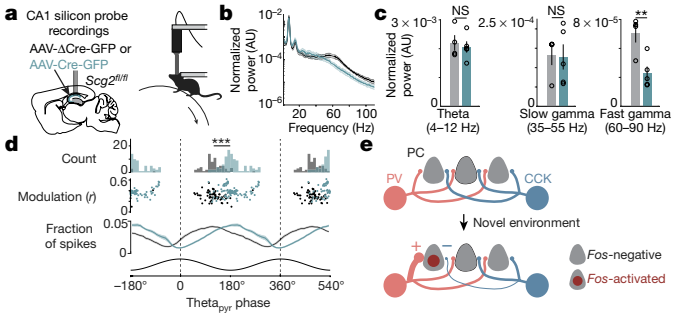

Fig. 6 | *Scg2* is required to maintain network rhythms in vivo. a, Schematic of silicon probe placement in CA1 pyramidal layer (left) and head-fixed awake-behaving setup (right). After AAV injections, mice were exposed to NE daily for 1–2 weeks before recordings. **b**, Normalized power spectra of network oscillations in running *Scg2*-WT (grey, $N = 4$) or *Scg2*-KO (green, $N = 5$) mice; one session per mouse. AU, arbitrary units. **c**, Mean of the normalized power spectra in theta, slow-gamma and fast-gamma bands during running as in **b**. Two-sided *t*-test, $^{**}P = 0.009$. **d**, Theta phase modulation of putative CA1 PCs. Two cycles of theta shown. Top, mean spike-triggered theta phase distributions for *Scg2*-WT (grey, $n = 67$) and *Scg2*-KO (green, $n = 103$) units. $^{***}P < 0.001$ bootstrap significance test of difference between circular means of the two distributions; 1,000 shuffles. Middle, mean theta phase and mean resultant length for each unit. Bottom, fraction of spikes in each theta phase bin (10° bins). **e**, Model depicting experience-dependent reorganization of perisomatic inhibitory networks upon *Fos* activation in CA1 PCs, where weights of PV-IN and CCK-IN synaptic inputs are bidirectionally modulated. Data are mean ± s.e.m. (**b**–**d**). Schematic image in **a** (left) adapted with permission from Paxinos & Franklin (ref. [32]).

were altered, with *Scg2*-KO mice displaying significantly lower fast gamma (60–90 Hz) power compared with *Scg2*-WT mice when running (Fig. 6b, c, Extended Data Fig. 10b, c). By contrast, the power of theta rhythms (4–12 Hz) and mean spike rates were not significantly different between *Scg2*-WT and *Scg2*-KO mice (Fig. 6b, c, Extended Data Fig. 10b–g).

Additionally, we found that PCs in *Scg2*-KO mice fired at a significantly different preferred $theta_{pyr}$ phase recorded in CA1 stratum pyramidale compared with *Scg2*-WT PCs (Fig. 6d). *Scg2*-KO cells tended to fire later in the $theta_{pyr}$ cycle, corresponding to the ascending phase of $theta_{pyr}$, whereas on average, *Scg2*-WT cells fired during the descending phase of $theta_{pyr}$ cycle (120.6° (*Scg2*-WT) and 187.3° (*Scg2*-KO) relative to the $theta_{pyr}$ peak (0°)). These results are consistent with the observed change in the balance between PV-IN and CCK-IN inputs upon loss of *Scg2*, as PV-INs and CCK-INs have been observed to fire during the descending and ascending phases of $theta_{pyr}$ oscillations, respectively[5,6].

Discussion

Despite the prevalence of *Fos*-activated neuronal networks across many regions of the brain, there is limited understanding of the circuit and molecular mechanisms by which these networks become persistently modified to support the consolidation of experiences over time. Moreover, whether FOS has a causal role in orchestrating circuit modifications and which of its many targets underlie these processes are not known. Here we reveal a bidirectional perisomatic inhibitory plasticity mechanism by which *Fos*-activated circuits are selectively reorganized in response to experience (Fig. 6e). We show that a FOS-to-SCG2 pathway is critical for this reorganization, and further define a role for SCG2 neuropeptidergic modulation in the entrainment of PC activity relative to theta phase and the regulation of gamma rhythms. These results, together with our finding that FOS is necessary for spatial learning, raise the possibility that *Fos*-dependent circuit reorganization is required to establish a network of cells for encoding and recalling memories.

Despite the broad axonal arborizations of PV-INs and CCK-INs within the CA1 pyramidal layer, distinct mechanisms appear to specifically reorganize and establish *Fos*-activated microcircuits compared with non-*Fos*-activated networks. That PV-IN and CCK-IN synaptic strengths are oppositely regulated by novel experience suggests functional consequences for this reorganization beyond a strictly homeostatic role in which increased PC activity is balanced by increased perisomatic inhibition within the network. Further work will be needed to understand how this experience-dependent shift in inhibitory control alters the temporal dynamics of network function in behaviourally adaptive ways.

For example, the peak and trough phases of theta rhythms measured in the CA1 pyramidal layer have been associated with memory encoding and recall, respectively, as the dominant source of inputs to CA1 cycles between entorhinal cortex and CA3[11,13]. *Fos*-mediated reorganization of inputs from PV-INs and CCK-INs, which themselves fire during different phases of the theta cycle, could provide a potential mechanism for altering a cell's eligibility to take part in these processes. We find that *Scg2*-expressing PCs fire preferentially during the descending phase of the theta cycle, which is when PV-INs also tend to fire[5,6], raising the possibility that the *Fos*-dependent recruitment of PV-mediated inhibition is critical for the formation of functional PV-pyramidal cell ensembles to support the consolidation of memories. In addition, *Scg2*-dependent regulation of gamma rhythms may be critical for transiently synchronizing the activity of populations of neurons within and across brain regions to facilitate information processing[12].

Additional distinctions in the molecular and physiological properties of PV-INs and CCK-INs may also contribute to the functional consequences of this shift. For example, experience-dependent strengthening of PV-mediated inhibition onto PCs may increase their spike threshold and impose narrower time windows for synaptic integration, which may allow them to better synchronize their firing[6,9]. Another key question is whether *Fos* or *Scg2* contribute to endocannabinoid signalling involving presynaptic CCK-INs[29,30].

While the specific in vivo cellular and learning-related neural activity features that lead to the induction of *Fos* during natural behaviours are a subject of active investigation[1,2], our findings indicate that *Fos* expression has an instructive role in orchestrating persistent circuit modifications, beyond serving as a marker of recent neural activity. In particular, FOS coordinates neuropeptidergic networks to modulate connectivity through its regulation of *Scg2*. In the brain, SCG2 has been reported to be mostly processed into its distinct neuropeptides[28,31], suggesting that individual SCG2-derived peptides probably mediate bidirectional perisomatic inhibitory plasticity. Although alternative mechanisms of SCG2-mediated inhibitory plasticity should also be examined[28], characterization of the specific SCG2-derived peptides that are involved, their pre- or post-synaptic sites of action, and the identity of their cognate G-protein-coupled receptors will be critical for further assessing the physiological functions of FOS–SCG2 signalling and the pathological consequences when this pathway is disrupted.

Online content

Any methods, additional references, Nature Research reporting summaries, source data, extended data, supplementary information, acknowledgements, peer review information; details of author contributions and competing interests; and statements of data and code availability are available at https://doi.org/10.1038/s41586-020-3031-0.

1. Josselyn, S. A. & Tonegawa, S. Memory engrams: Recalling the past and imagining the future. *Science* **367**, eaaw4325 (2020).
2. Tanaka, K. Z. et al. The hippocampal engram maps experience but not place. *Science* **361**, 392–397 (2018).
3. Greenberg, M. E. & Ziff, E. B. Stimulation of 3T3 cells induces transcription of the c-*fos* proto-oncogene. *Nature* **311**, 433–438 (1984).
4. Freund, T. F. & Katona, I. Perisomatic inhibition. *Neuron* **56**, 33–42 (2007).
5. Klausberger, T. et al. Complementary roles of cholecystokinin- and parvalbumin-expressing GABAergic neurons in hippocampal network oscillations. *J. Neurosci.* **25**, 9782–9793 (2005).
6. Bartos, M. & Elgueta, C. Functional characteristics of parvalbumin- and cholecystokinin-expressing basket cells. *J. Physiol.* **590**, 669–681 (2012).
7. Yap, E. L. & Greenberg, M. E. Activity-regulated transcription: bridging the gap between neural activity and behavior. *Neuron* **100**, 330–348 (2018).
8. Ryan, T. J., Roy, D. S., Pignatelli, M., Arons, A. & Tonegawa, S. Engram cells retain memory under retrograde amnesia. *Science* **348**, 1007–1013 (2015).
9. Glickfeld, L. L. & Scanziani, M. Distinct timing in the activity of cannabinoid-sensitive and cannabinoid-insensitive basket cells. *Nat. Neurosci.* **9**, 807–815 (2006).
10. Hefft, S. & Jonas, P. Asynchronous GABA release generates long-lasting inhibition at a hippocampal interneuron-principal neuron synapse. *Nat. Neurosci.* **8**, 1319–1328 (2005).
11. Buzsáki, G. Theta oscillations in the hippocampus. *Neuron* **33**, 325–340 (2002).
12. Buzsáki, G. & Wang, X. J. Mechanisms of gamma oscillations. *Annu. Rev. Neurosci.* **35**, 203–225 (2012).
13. Hasselmo, M. E. & Stern, C. E. Theta rhythm and the encoding and retrieval of space and time. *Neuroimage* **85**, 656–666 (2014).
14. Sørensen, A. T. et al. A robust activity marking system for exploring active neuronal ensembles. *eLife* **5**, e13918 (2016).
15. Fenno, L. E. et al. Targeting cells with single vectors using multiple-feature Boolean logic. *Nat. Methods* **11**, 763–772 (2014).
16. Taniguchi, H. et al. A resource of Cre driver lines for genetic targeting of GABAergic neurons in cerebral cortex. *Neuron* **71**, 995–1013 (2011).
17. Roth, B. L. DREADDs for neuroscientists. *Neuron* **89**, 683–694 (2016).
18. Xue, M., Atallah, B. V. & Scanziani, M. Equalizing excitation–inhibition ratios across visual cortical neurons. *Nature* **511**, 596–600 (2014).
19. Vierbuchen, T. et al. AP-1 transcription factors and the BAF complex mediate signal-dependent enhancer selection. *Mol. Cell* **68**, 1067–1082 (2017
20. Fleischmann, A. et al. Impaired long-term memory and NR2A-type NMDA receptor-dependent synaptic plasticity in mice lacking c-Fos in the CNS. *J. Neurosci.* **23**, 9116–9122 (2003)
21. Hrvatin, S. et al. Single-cell analysis of experience-dependent transcriptomic states in the mouse visual cortex. *Nat. Neurosci.* **21**, 120–129 (2018).
22. Sanz, E. et al. Cell-type-specific isolation of ribosome-associated mRNA from complex tissues. *Proc. Natl Acad. Sci. USA* **106**, 13939–13944 (2009).
23. Skene, P. J. & Henikoff, S. An efficient targeted nuclease strategy for high-resolution mapping of DNA binding sites. *eLife* **6**, e21856 (2017).
24. Mo, A. et al. Epigenomic signatures of neuronal diversity in the mammalian brain. *Neuron* **86**, 1369–1384 (2015).
25. Bloodgood, B. L., Sharma, N., Browne, H. A., Trepman, A. Z. & Greenberg, M. E. The activity-dependent transcription factor NPAS4 regulates domain-specific inhibition. *Nature* **503**, 121–125 (2013).
26. Hensch, T. K. Bistable parvalbumin circuits pivotal for brain plasticity. *Cell* **156**, 17–19 (2014).
27. Nedivi, E., Hevroni, D., Naot, D., Israeli, D. & Citri, Y. Numerous candidate plasticity-related genes revealed by differential cDNA cloning. *Nature* **363**, 718–722 (1993).
28. Fischer-Colbrie, R., Laslop, A. & Kirchmair, R. Secretogranin II: molecular properties, regulation of biosynthesis and processing to the neuropeptide secretoneurin. *Prog. Neurobiol.* **46**, 49–70 (1995).
29. Földy, C., Malenka, R. C. & Südhof, T. C. Autism-associated neuroligin-3 mutations commonly disrupt tonic endocannabinoid signaling. *Neuron* **78**, 498–509 (2013).
30. Hartzell, A. L. et al. NPAS4 recruits CCK basket cell synapses and enhances cannabinoid-sensitive inhibition in the mouse hippocampus. *eLife* **7**, e35927 (2018).
31. Weiler, R. et al. Chromogranins in rat brain: characterization, topographical distribution and regulation of synthesis. *Brain Res.* **532**, 87–94 (1990).
32. Franklin, K. B. J. & Paxinos, G. *The Mouse Brain in Stereotaxic Coordinates* 3rd edn (Academic Press/Elsevier, 2007).

Methods

No statistical methods were used to predetermine sample size. The investigators were not blinded to allocation during experiments and outcome assessment, except where specified below.

Mice

Mice were handled according to protocols approved by the Harvard University Standing Committee on Animal Care and were in accordance with federal guidelines. The following mouse lines were used: PV-Cre (JAX 017320), CCK-Cre (JAX 012706), PV-Flpo (JAX 022730), C57BL/6J (JAX 000664), Ai14 (JAX 007914), Ai65 (JAX 021875), CaMK2a-Cre (JAX 005359), *Rpl22*-Ribotag (JAX 029977), LSL-Sun1-sfGFP-Myc (JAX 021039), Emx1-Cre (JAX 005628), Dlx5/6-Flp (ref. [33]), $Fos^{fl/fl}$;$Fosb^{fl/fl}$;$Junb^{fl/fl}$ (refs. [19,20,34]), *Fos*-FlagHA (ref. [19]), *Npas4*-FlagHA (ref. [35]), C57BL/6N (Charles River Laboratories; for embryonic cultured neurons) and $Scg2^{fl/fl}$ (described here).

The conditional-knockout $Scg2^{fl/fl}$ mouse was generated with the help of the Harvard Genome Modification Facility (L. Wu). In brief, *LoxP* sites were introduced flanking the entire coding exon of *Scg2*. *Cas9* mRNA, two sgRNAs each targeting a site for *LoxP* insertion, and two 150–200-bp single-stranded oligonucleotides for repair were injected into C57BL/6J mouse zygotes. Correct *cis* insertion of both *LoxP* sites were verified by standard PCR and Sanger sequencing. A founder male was bred to C57BL/6J mice for at least three generations before experimental use.

Mice were housed in ventilated micro-isolator cages in a temperature- and humidity-controlled environment under a standard 12 h light/dark cycle, with food and water provided ad libitum. Both male and female littermate mice were used in similar proportions and divided between control and experimental groups for all experiments conducted. For in vivo silicon probe recordings and Morris water maze experiments, only male littermate mice, housed in a reverse 12 h light/dark cycle, were used.

Novel environment paradigm

Animals at weaning age and above (> P21) were placed in a large opaque cage (0.66 m × 0.46 m × 0.38 m) in a group with other mice, equipped with an assortment of enrichment including a running wheel, mazes, tunnels, ladders, huts, swings, and different kinds of animal bedding. Rodent pellets were hidden in mazes to encourage spatial exploration. Mice were placed in a specific environment for 12–24 h. The environments were subsequently significantly changed daily to provide novel multisensory experiences and transcriptionally activate a larger proportion of neurons.

Intraperitoneal injections

For kainic acid treatment, mice were injected intraperitoneally with kainic acid (Sigma Aldrich, K0250) reconstituted in 0.001 N NaOH in PBS at 5–10 mg kg^{-1} for electrophysiology or 15–20 mg kg^{-1} for genomic or histological analyses. We used 1–1.5 h or 2–3 h kainic acid as the time point for capturing the peak of immediate early gene (for example, *Fos*) RNA or protein induction, respectively. We used 4 h kainic acid as the time point for capturing the peak of nascent RNA induction for late-response genes, as nascent RNA molecules are first present in the nuclei (FFJ snRNA-seq). Subsequently, for ribosome-associated mature RNA from late-response genes, we used a 6 h kainic acid time point as we reasoned that more mature RNA tends to associate with ribosomes at this later time point (Ribotag). For electrophysiology, mice were sacrificed 24 h after kainic acid injection to allow sufficient time for the expression and action of activity-dependent genes but far in advance of any measurable seizure-related cellular toxicity (see Extended Data Fig. 2m–q).

For chemogenetic activation experiments, CNO (Sigma C0832) reconstituted in 0.4% DMSO in PBS was injected intraperitoneally at 5 mg kg^{-1} in mice 24 h before electrophysiology.

Stereotaxic surgery

For acute hippocampal slice recordings, mice aged P13–15 of equal proportion male and female were anaesthetized by isoflurane inhalation (2% induction, 1% maintenance) and positioned within a stereotaxic frame (Kopf Model 963). Animal temperature was maintained at 37 °C by a heat pad. All surgeries were performed according to protocols approved by the Harvard University Standing Committee on Animal Care and were in accordance with federal guidelines. Fur around the scalp area was removed using a shaver and sterilized with three alternating washes with betadine and 70% ethanol. A burr hole was drilled through the skull above the CA1 region of hippocampus (medial/lateral, ML: ± 2.9 mm; anterior/posterior, AP: −2.4 mm; dorsal/ventral, DV: −2.8 mm) to allow for specific targeting of this region with a glass pipette pulled to a tip diameter of approximately 50 µm. AAV virus (1,000 nl) was injected at 150 nl min^{-1} and the pipette was left in place for 5 min upon completion of viral infusion to allow for viral spreading. All animals were given postoperative analgesic (flunixin, 2.5 mg kg^{-1}) as well as additional injections at 12-h intervals for the 72 h following surgery.

Viral vectors and titres

All AAVs used were prepared in the Boston Children's Hospital Viral Core and were of serotype AAV2/1. For sparse transductions, viruses were injected at 1×10^8 genome copies (gc) per hippocampal hemisphere. For dense transductions, viruses were injected at 2×10^9 gc per hippocampal hemisphere. The viral vectors and original titres are as follows: pAAV-EF1a-DIO-hChR2(H134R)-EYFP (Addgene 20298, 1.75×10^{13} gc ml^{-1}), pAAV-EF1a-fDIO-hChR2(H134R)-EYFP (Addgene 55639, 1.39×10^{13} gc ml^{-1}), pAAV-hSyn-Con/Fon-hChR2-EYFP (Addgene 55645, 2.25×10^{14} gc ml^{-1}), pAAV-pRAM-tTA::TRE-NLS-mKate2-WPREpA (Addgene 84474, 2.25×10^{13} gc ml^{-1}), pAAV-CAG-Cre-GFP (M. During, Ohio State University, 1.75×10^{13} gc ml^{-1}), pAAV-CAG-Cre-mCherry (this Article, 9.10×10^{12} gc ml^{-1}), pAAV-CAG-Cre-mTagBFP2 (this Article, 2.97×10^{12} gc ml^{-1}), pAAV-CAG-deltaCre-GFP (this Article, 2.79×10^{12} gc ml^{-1}), pAAV-FlpOFF-u6-shRNA-CAG-mCherry (this Article): Control shRNA (ACTTACGCTGAGTACTTCG) (5.08×10^{13} gc ml^{-1}), *Inhba* (CCTTCCACTCA ACAGTCATT) (4.62×10^{13} gc ml^{-1}), *Bdnf* (GAATTGGCTGGCGATTCATA) (6.97×10^{13} gc ml^{-1}), *Pcsk1* (GATAATGATCATGATCCATT) (6.02×10^{12} gc ml^{-1}), *Nptx2* (GAAGACATTGCCTGAGCTGT) (1.30×10^{12} gc ml^{-1}), *Scg2*#1 (GCAGACAAGCACCTTATGAA) (8.11×10^{11} gc ml^{-1}), *Scg2*#2 (CCCTTGA TTCTCAGTCTATT) (2.75×10^{13} gc ml^{-1}), *Rgs2* (GCTCCCAAAGAGA TAAACAT) (6.14×10^{12} gc ml^{-1}), pAAV-CaMKIIa-mCherry (this Article, 3.80×10^{12} gc ml^{-1}), pAAV-CaMKIIa-hM3D_{Gq}-T2A-mCherry (this Article, 1.20×10^{12} gc ml^{-1}), pAAV-hSyn-FlpOFF-Kir2.1-T2A-mCherry (this Article, 2.26×10^{12} gc ml^{-1}), pAAV-hSyn-FlpOFF-Kir.2.1(Mutant)-T2A-mCherry[18] (this Article, 1.28×10^{12} gc ml^{-1}), pAAV-u6(Frt)-*Scg2*#1 shRNA-CAG-Sc g2-rescue (shRNA-resistant)-1×HA-T2A-mCherry-Frt-SV40 (this Article, 1.88×10^{12} gc ml^{-1}), pAAV-CAG-DIO-Scg2(WT)-3×HA-bGH polyA (this Article, 8.22×10^{13} gc ml^{-1}), pAAV-CAG-DIO-Scg2(9AA Mutant)-3× HA-bGH polyA (this Article, 6.13×10^{13} gc ml^{-1}), pAAV-CAG-Scg2(WT)-1× HA-T2A-mCherry-bGH polyA (this Article, 1.08×10^{13} gc ml^{-1}) and pAAV-CAG-Scg2(9AA Mutant)-1×HA-T2A-mCherry-bGH polyA (this Article, 3.71×10^{12} gc ml^{-1}).

For lentiviral production of shRNAs, lentiviral backbone pSicoR (Addgene 11579) was used for cloning of all shRNAs. A total of 10 mg of lentiviral plasmid was transfected into 293T cells in a 10-cm dish along with third generation packaging vectors pMD2.G (Addgene 12259), pRSV-rev (Addgene 12253) and pMDLg/pRRE (Addgene 12251). At 12–16 h following transfection, 293T cells were switched to Neurobasal media (Gibco) containing B27 supplement (2%), penicillin (50 U ml^{-1}), streptomycin (50 U ml^{-1}) and gluta-MAX (1 mM). Supernatant containing virus was collected at 36 h post-transfection, spun down to remove cellular debris at 1,000*g* for 5 min, and added directly to cultured neurons.

Acute slice preparation

Transverse hippocampal slices were prepared from mice aged P23–P32. Mice were anaesthetized with ketamine/xylazine and transcardially perfused with ice-cold choline-based artificial cerebrospinal fluid (choline-ACSF) equilibrated with 95% O_2/5% CO_2 consisting of (in mM): 110 choline chloride, 25 $NaHCO_3$, 1.25 NaH_2PO_4, 2.5 KCl, 7 $MgCl_2$, 25 glucose, 0.5 $CaCl_2$, 11.6 sodium L-ascorbate and 3.1 sodium pyruvate. Cerebral hemispheres were quickly removed and placed into ice-cold choline-ACSF. Tissue was rapidly blocked and transferred to a vibratome (Leica VT1000). Dorsal hippocampal slices of 300-µm thickness were collected in a holding chamber containing ACSF consisting of (in mM): 127 NaCl, 25 $NaHCO_3$, 1.25 NaH_2PO_4, 2.5 KCl, 1 $MgCl_2$, 10 glucose and 2 $CaCl_2$. For all solutions, pH was set to 7.2 and osmolarity to 300 mOsm. Slices were incubated at 32 °C for 20 min and maintained at room temperature (22 °C) for 30 min before recordings began. All recordings were performed at room temperature within 4–5 h of slice preparation. AAV transduction was assessed by epifluorescence. For experiments where sparse transduction of CA1 was intended, slices with 10–30% of CA1 neurons infected were used, and slices showing >30% of CA1 neurons infected were discarded from further analysis. For optogenetic stimulation experiments, slices showing ChR2 spread across the entire CA1 were used, and slices showing partial expression of ChR2 across CA1 were discarded from further analysis. For all experiments, slices were discarded if AAV transduction spread to CA3 and/or dentate gyrus regions.

Ex vivo electrophysiology

For whole-cell voltage-clamp recordings, a CsCl-based internal solution consisting of (in mM): 135 CsCl, 3.3 QX314-Cl, 10 HEPES, 4 MgATP, 0.5 NaGTP, 8 Na_2-phosphocreatinine, 1.1 EGTA and 0.1 $CaCl_2$ (pH 7.2, 290 mOsm) was used for all IPSC measurements. A Cs^+-methanesulfonate internal solution consisting of (in mM): 127 $CsMeSO_3$, 10 CsCl, 10 HEPES, 0.5 EGTA, 2 $MgCl_2$, 0.16 $CaCl_2$, 2 MgATP, 0.4 NaGTP, 14 Na_2-phosphocreatinine, and 2 QX314-Cl (pH 7.2, 295 mOsm) was used for all EPSC measurements. A K^+-based internal solution consisting of (in mM): 142 K^+-gluconate, 4 KCl, 10 HEPES, 4 MgATP, 0.3 NaGTP, 10 Na_2-phosphocreatinine, and 1.1 EGTA (pH 7.2, 280 mOsm) was used for all current-clamp recordings. Membrane potentials were not corrected for liquid junction potential (which were experimentally measured as −5 mV for CsCl-based internal solution, and 60 mV for K-gluconate-based internal solution). In all recordings, neurons were held at −70 mV with patch pipettes made with borosilicate glass with filament (Sutter BF150-86-7.5) with 2–4 MΩ open pipette resistance. For all dual whole-cell recordings of pairs of CA1 pyramidal neurons, recording from neighbouring neurons increased the probability that both neurons received synaptic inputs from the same population of inhibitory axons, and ensured that both neurons were exposed to an identical stimulus magnitude and intensity.

Recordings were made on an upright Olympus BX51 WI microscope with an infrared CCD camera (Dage-MTI IR-1000) and 60X water immersion objective (Olympus Lumplan Fl/IR 60×/0.90 numerical aperture). Neurons were visualized using video-assisted infrared differential interference contrast, and fluorescence was identified by epifluorescence driven by a light-emitting diode (Excelitas XCite LED120). For photostimulation of ChR2-expressing boutons, 470-nm blue light was delivered from the LED through the reflected light fluorescence illumination port and the 60× objective. Pulses were delivered at 0.4 Hz. Pulse duration (0.1–0.2 ms) and intensity (1.3–5.9 mW/mm^2) were adjusted for each recording to evoke small but reliable monosynaptic IPSCs. No pharmacology was used for optogenetic stimulation experiments.

For electrical stimulation experiments, electrical current was delivered via a theta glass stimulus electrode placed in the centre of stratum pyramidale or stratum radiatum within 150–200 µm of the recorded neuron pair. The stimulus strength was the minimum required to generate small but reliable currents in both neurons. IPSCs were pharmacologically isolated via the addition of 10 µM NBQX (Tocris 1044) and 10 µM (*R*)-CPP (Tocris 0247) to the ACSF perfusion. For pharmacological isolation of CCK-IPSCs specifically, in addition to blocking excitatory currents, PV-IPSCs were blocked using 0.4 µM of ω-agatoxin IVA, a selective antagonist for P/Q-type calcium channels (Peptides International, PAG-4256-s). EPSCs were pharmacologically isolated by adding 10 µM gabazine (Tocris 1262).

For simultaneous dual whole-cell recordings, we determined that the IPSCs measured were monosynaptic as the addition of NBQX and (*R*)-CPP in the bath did not alter the onset latency of the IPSCs. For the paired IN-to-CA1 pyramidal neuron recordings, the monosynaptic nature of the IPSCs was confirmed based on the expected onset latency of 1–3 ms in slice.

Data acquisition and analysis. Data were low-pass filtered at 4 kHz and sampled at 10 kHz with an Axon Multiclamp 700B amplifier, and digitized with an Axon Digidata 1440A data acquisition system controlled using Clampex 10.6 (Molecular Devices). Experiments were discarded if holding current exceeded -500 pA, or if series resistance was greater than 30 MΩ. For the dual whole-cell recordings of CA1 pyramidal neurons, recordings were discarded if series resistance differed by more than 30% between the two neurons. The recorded traces were analysed using Clampfit 10.6 (Molecular Devices) or Axograph (1.7.6). All current amplitude measurements are expressed as mean ± s.e.m., or as differences in amplitudes between a pair of neurons normalized to the total amplitudes of both neurons (ΔIPSC/ΣIPSC). The differences (ΔIPSC) are calculated between a fluorescently labelled (that is, manipulated) cell minus a control (that is, non-manipulated) cell, such that a positive number indicates a larger IPSC amplitude in the manipulated cell compared to the control cell, and vice versa.

Sample sizes were not predetermined and are similar to those reported in the literature[18,25,35]. Previous work suggests that in general, approximately 15–20 pairs of neurons (*n*) collected from 3–5 animals (*N*) are sufficient for each experiment. Most data, except where specified (Fig. 4c–e), were not collected blind to genotype or conditions, but all offline analyses were conducted blind. All statistical analyses were performed using Prism 8 (Graphpad). Data were tested for normality using the D'Agostino–Pearson, Shapiro–Wilk and Kolmogorov–Smirnov normality tests. For simultaneous dual whole-cell recordings of pyramidal neurons, two-sided *t*-testsor ordinary one-way ANOVA, with multiple comparisons correction, were used. For recordings of unitary connections, non-parametric two-sided Mann–Whitney tests were used. A mixed model was used to confirm that findings were not driven by a single mouse. The numbers of cells recorded per animal were capped to ensure even sampling across mice comprising a dataset (for example, if $n = 20$ pairs were obtained using $N = 4$ mice, 4–6 pairs were used per mouse).

Histology

Mice were anaesthetized with 10 mg ml^{-1} ketamine and 1 mg ml^{-1} xylazine in PBS by intraperitoneal injection. When fully anaesthetized, the animals were transcardially perfused with 5 ml ice-cold PBS followed by 20 ml of cold 4% PFA in PBS. Brains were dissected and post-fixed for 24 h at 4 °C in 4% PFA, followed by three washes (each for 30 min) in cold PBS. Coronal sections (40-µm thick) were subsequently cut using a vibratome (Leica VT1000) and stored in PBS at 4 °C until further use. For immunostaining, slices were permeabilized for 30 min at room temperature in PBS containing 0.3% Triton X-100. Slices were blocked for 1 h at room temperature with PBS containing 0.3% Triton X-100, 2% normal donkey serum and 0.1% fish gelatin. Slices were incubated in primary antibodies diluted in blocking solution at 4 °C for 48 h: rabbit anti-FOS antibody (Synaptic Systems 226003, 1:3,000), mouse anti-FOS (Abcam ab208942, 1:1,000), rabbit anti-NPAS4[36] (1:1,000), rabbit anti-FOSB (Cell Signaling Technology 2251S, 1:1,000), rabbit anti-JUNB

(Cell Signaling Technology 3753S, 1:1,000), rat anti-HA (Sigma ROAHAHA, 1:500), rabbit anti-PV (Swant PV27, 1:10,000), rabbit anti-cleaved caspase-3 (Cell Signaling Technology 9661S, 1:1,000) and mouse monoclonal anti-NeuN (Millipore Sigma MAB377, 1:1,000). Slices were then washed three times with PBS each for 10 min at room temperature, incubated for 2 h at room temperature with secondary antibodies conjugated to Alexa Fluor dye (Life Technologies; rat Alexa Fluor 555 (A21434), rabbit Alexa Fluor 488 (A21206), rabbit Alexa Fluor 555 (A31572), rabbit Alexa Fluor 647 (A31573), mouse Alexa Fluor 555 (A31570), mouse Alexa Fluor 647 (A31571), 1:250), and washed three times with PBS. Slices were then mounted in DAPI Fluoromount-G (Southern Biotech) and imaged on a virtual slide microscope (Olympus VS120).

smRNA-FISH

For sample preparation, hippocampal hemispheres from mice were fresh- or fixed-frozen in Tissue-Tek Cryo-OCT compound (Fisher Scientific) on dry ice and stored at −80 °C until further use. Hippocampi were sectioned at a thickness of 15–20 µm and RNAs were detected by RNAscope (Advanced Cell Diagnostics) using the manufacturer's protocol. Probes for *Fos*, *Fosb* and *Junb* were custom designed with Advanced Cell Diagnostics specifically to detect exons excised upon Cre recombinase expression. The following probes were used: Mm-*Cre* (546951), Mm-*Fos* (584741), Mm-*Fosb* (584751), Mm-*Junb* (584761), Mm-*Scg2* (477691) and Mm-*Scg2* intron (859141). All in situ hybridizations were imaged using a confocal microscope (Zeiss Imager Z2) and analysed in ImageJ (Fiji v1.0).

Validation of loss of *Fos*, *Fosb* and *Junb* in the FFJ mouse line

Efficient excision of *Fos*, *Fosb* and *Junb* upon Cre expression was confirmed at the RNA level using smRNA-FISH and at the protein level using immunostaining for each of the three genes. The *Fos* conditional-knockout allele allows for deletion of three exons, including the last exon encoding the 3′ UTR, upon Cre expression, whereas the *Fosb* and *Junb* conditional-knockout alleles are single-exon deletions (Exon 2 of 4 for *Fosb*; coding region only for *Junb*). As such, for smRNA-FISH, the probes were custom designed to specifically target the excised exons. Note that FFJ snRNA-seq detects the 3′ ends of transcripts, resulting in comparatively sparse coverage of full transcripts particularly at the 5′ end of genes. This approach can therefore be used to confirm the deletion of *Fos* but not *Fosb* and *Junb* due to the design of the conditional-knockout alleles, which leaves intact the 3′ transcripts of *Fosb* and *Junb* upon Cre excision, resulting in non-trivial tags during library preparation.

Cultured hippocampal neurons and RNA isolation for RT–qPCR or bulk RNA sequencing

Embryonic hippocampi from C57BL/6N (Charles River Laboratories) or *Scg2*$^{fl/fl}$ mice were dissected at age E16.5 or P0, respectively, then dissociated with papain (Sigma Aldrich 10108014001). Cultures were generated by combining multiple embryos of both males and females (mixed sex cultures). Papain digestion was terminated with the addition of ovomucoid (trypsin inhibitor; Worthington). Cells were gently triturated with a P1000 pipette and passed through a 40-µm filter. Neurons were plated onto cell culture dishes pre-coated overnight with poly-D-lysine (20 mg ml^{-1}) and laminin (4 mg ml^{-1}). Neurons were grown in Neurobasal medium (GIBCO) containing B27 supplement (2%), penicillin (50 U ml^{-1}), streptomycin (50 U ml^{-1}) and gluta-MAX (1 mM). Neurons were grown in incubators maintained at 37 °C and a CO_2 concentration of 5%. In all experiments, independent replicates were generated from dissections of mice on different days. Neurons were cultured in 6-well dishes at 1 million neurons per well. Neurons were transduced with lentiviral supernatant on days in vitro 2 (DIV2) by replacing one third of Neurobasal media with lentiviral supernatant. Fresh media was added at DIV4 (one fourth total volume). At DIV7, neurons were depolarized with 55 mM KCl for 1 h or 6 h to assess immediate early or late-response activity-dependent genes, respectively, and RNA was subsequently harvested by gentle agitation with Trizol (Life Technologies 15596026) at room temperature for 2 min. The RNeasy Micro kit (Qiagen 74004) was used according to the manufacturer's instructions to purify DNA-free RNA. For quantitative PCR with reverse transcription (RT–qPCR), RNA was converted to cDNA using 200 ng of RNA with the high-capacity cDNA reverse transcription kit (Life Technologies 4374966). RT–qPCR was performed with technical triplicates and mapped back to relative RNA concentrations using a standard curve built from a serial dilution of cDNA. Data were collected using a QuantStudio 3 qPCR machine (Applied Biosystems). For bulk RNA-sequencing, 100 ng of RNA was used to generate libraries following rRNA depletion (NEBNext, E6310X) according to the manufacturer's instructions (NEBNext, E7420). The 75-bp reads were generated on the Illumina Nextseq 500 and subsequently analysed using a standardized RNA-seq data analysis pipeline[37].

Morris water maze behavioural paradigm

FFJ littermate mice (8–14-week-old) were injected with AAV-Cre-GFP or AAV-ΔCre-GFP bilaterally into the CA1 (Kopf Model 1900; stereotaxic coordinates of AP −2 mm, ML ± 1.5 mm, DV −1.3 mm from bregma). Mice were given injections of dexamethasone and buprenorphine SR, and allowed to recover for 1–2 weeks before behavioural training. The maze (97 cm in diameter) was filled with room-temperature water made opaque by the addition of tempera to a height of 40 cm. A hidden platform of 7-cm diameter was placed 14 cm from the edge of the maze and submerged 1 cm below the water level. Distal cues were placed on all four walls of the testing room. Mice were trained in two blocks per day for four consecutive days (days 1–4). Each block consisted of four trials. In each trial, mice were placed at one of eight (randomized) start positions spaced evenly along half of the circumference of the pool opposite the half of the pool that contained the hidden platform. Mice were given 60 s to find the platform. If mice did not find the platform within this time, they were guided to the platform by the experimenter and allowed to sit for 10 s. Mice were subsequently removed from the platform and placed in a warmed cage to dry. Two 40-s probe trials were conducted one day after training (day 5) during which the platform was removed. The swim paths of the mice were recorded by a video camera suspended several feet above the centre of the maze. The experimenter was blinded to the genotype of the mice. Mice that did not swim ('floaters') were excluded from further analysis.

Analysis. All video tracking and analysis was carried out using custom MATLAB code. Swim trajectories for each trial were tracked semi-automatically and manually corrected. For one mouse in the study, due to tracking issues the trials in the second block on the first day (trials 5–8) were excluded from the analysis—therefore for that mouse only four trials were considered in the performance metric on day 1. For analyses of swim speeds and path lengths, the mean was computed for each mouse across all trials on the first two days in order to control for similar levels of exploration.

Ribosome-associated mRNA profiling

Hippocampal tissue was rapidly dissected from mice and subsequently used for isolation of ribosome-bound mRNAs. Immunopurification of ribosome-bound mRNAs was performed as previously described[22], with 10 mM Ribonucleoside Vanadyl Complex (NEB S1402S) present in the lysis buffer and using the mouse monoclonal anti-HA antibody (Sigma HA-7, H3663, 12 µg per immunoprecipitation). A small fraction of lysate before the immunoprecipitation was used as input for each sample. All RNA samples (20 ng for CaMK2a; 2.5 ng for PV) with sufficient integrity as analysed by 2100 Bioanalyzer were SPIA-amplified with the Ovation RNA-seq System V2 (NuGEN). Subsequently, SPIA-amplified cDNA (1 µg) was fragmented to a length of approximately 400 bp using a Covaris S2 sonicator (Acoustic Wave Instruments). Fragmented cDNA (100 ng)

was used to generate Illumina-compatible sequencing libraries using the Ovation Ultralow System V2 (NuGEN). Libraries were sequenced on the Illumina NextSeq 500 (Basespace) for 75 bp single-end reads to a depth of 20–40 million reads per sample.

Analysis. Analyses of Ribotag sequencing were performed for each sample at each stimulation time point as previously described[38]. In brief, raw sequencing reads ≤ 75 bp in length were 3′-trimmed to a uniform 70 bp (ignoring the ~0.1% of reads that were shorter than this) and filtered for quality control. These were then mapped strand-nonspecifically to the mm10 genome (GRCm38) using the Burrows-Wheeler Aligner (bwa), allowing up to 2 mismatches and no gaps. In addition to the usual assembled chromosomes, alignment targets included mitochondrial DNA and a library of ~7 million short splice-junction sequences. Typically, 75–80% of reads were mappable; nonuniquely mapped reads were discarded, as were any that mapped to loci of rRNA genes (from RepeatMasker).

Genic features were based on exonic loci from the NCBI RefSeq annotation for mm10. Mean expression density across a gene's exons was taken as a proxy for its expression level. However, noncoding genes, some of which expressed quite highly and variably from one sample to the next, were excluded from these analyses. The splice-junction target sequences for each gene comprised subsequences of minimal length of all possible concatenations of two or more ordered exons such that their boundaries would be crossed by 70-bp reads. This provided an exhaustive, nonredundant set of predictable exon-junction-spanning loci which typically accounted for ~20% of all exonic reads from mature messages.

Differential expression analyses employed edgeR in R to compare transcript levels in all biological-replicate samples at 6 h of kainic acid stimulation to the unstimulated samples. A gene's expression level was flagged as significantly changed if (1) the Benjamini–Hochberg-corrected *P* value (*q* value) for the change, as calculated by edgeR, was consistent with an FDR of ≤ 0.005, and (2) it passed a modest background filter (total number of reads ≥ 4 across all compared samples).

Nuclei isolation

Hippocampal tissue from mice was rapidly dissected and dounce homogenized. Dounce homogenization was performed in buffer HB (0.25 M sucrose, 25 mM KCl, 5 mM $MgCl_2$, 20 mM Tricine-KOH, pH 7.8 supplemented with protease inhibitors, 1 mM DTT, 0.15 mM spermine and 0.5 mM spermidine) with a tight pestle for 20 strokes in a 1.5 ml total volume. Tissue was then supplemented with 96 µl 5% IGEPAL CA-630 and dounced an additional 5 strokes with a tight pestle. Homogenate was then filtered through a 40-µm strainer to remove large debris and collected in a 15 ml conical tube before the addition of 3.5 ml buffer HB and 5 ml working solution (50% iodixanol with 25 mM KCl, 5 mM $MgCl_2$, 20 mM Tricine-KOH pH 7.8 supplemented with protease inhibitors, DTT, spermine and spermidine). Homogenized tissue was underlaid with 1 ml of 30% iodixanol and 1 ml of 40% iodixanol (diluted from working solution) solutions. Samples were centrifuged at 10,000*g* for 18 min. Nuclei were collected in a 70 µl or 250 µl volume at the 30/40% iodixanol interface for 10X Genomics and CUT&RUN protocols, respectively.

FFJ snRNA-seq

FFJ snRNA-seq was performed with the 10X Genomics Chromium Single Cell Kit (v3). Approximately 7,000–10,000 nuclei were added to the reverse-transcription mix before loading on the microfluidic chip. Each snRNA-seq sample consists of pooled nuclei from two mice. All downstream steps for the cDNA synthesis, cDNA amplification and library preparation were performed according to the manufacturer's instructions (10X Genomics). All samples were sequenced on Illumina NextSeq 500 (Basespace) with 58 bp (read 1), 26 bp (read 2) and 8 bp (index).

Analysis. Initial FASTQ files were generated using the standard bcl2fastq Illumina pipeline, and gene expression tables for each barcode were generated using the CellRanger 3.0.0 pipeline according to instructions provided by 10X Genomics. AAV-transduced cells were detected by the presence of mRNA species mapping to the WPRE-bGH polyA sequence present in all AAVs used in this study. WPRE transcripts were PCR amplified using custom primers. Gene expression tables were then imported into R and analysed using custom written functions as well as the Seurat (v3) package. Exclusion criteria: Nuclei were removed from the dataset if they contained fewer than 500 discovered genes or had greater than 5% of reads mapping to mitochondrial genes. General analysis parameters: Raw UMI counts were normalized to 10^4 UMIs per cell (that is, tags per ten thousand, TPT). Nuclei from all Cre (or all ΔCre) mice were merged for the purposes of dimensionality reduction and clustering. Highly variable genes were identified using the FindVariableFeatures function (selection.method = 'vst', nFeatures = 2000), which identifies the 2,000 most variable genes amongst the analysed nuclei. Principal component analysis based on the 2,000 most variable genes was performed using the RunPCA function to reduce the dimensionality of the dataset. The top 20 principal components were retained and projected into a 2-dimensional space using the uniform manifold approximation and projection (UMAP) algorithm implemented using the RunUMAP function (n.neighbours = 50, min.dist = 0.5). The following genes were used as a guide to assign cell type identities to the graph-based clusters: pan-excitatory neurons (*Slc17a7*); CA1 excitatory neurons (*Fibcd1*, *Mpped1*); CA3 excitatory neurons (*Spock1*, *Cpne4*); excitatory dentate gyrus (*Prox1*, *C1ql2*); pan-inhibitory INs (*Gad2*, *Slc32a1*); Sst^+ INs (*Sst*); $Pvalb^+$ INs (*Pvalb*); Vip^+ INs (*Vip*); Cck^+ INs (*Cck*); $Nos1^+$ INs (*Nos1*), Npy^+ INs (*Npy*), oligodendrocytes (*Aspa*, *Opalin*, *Gjb1*); oligodendrocyte precursor cells (*Gpr17*, *C1ql1*); microglia (*Cx3cr1*, *C1qc*); endothelial cells (*Ly6c1*, *Cldn5*); astrocytes (*Cldn10*, *Gjb6*, *Gfap*)[21,39,40]. Differential gene expression analysis: Statistical significance of gene expression changes for all genes detected in greater than 5% of respective untransduced control cells for Cre or ΔCre samples was calculated using the Wilcoxon rank-sum test implemented through the FindMarkers function (logfc.threshold = 0.01, pseudocount.use = 0.001). Violin plots were generated using the VlnPlot function with default parameters, and heatmaps were generated using a custom written function in R. Heatmaps display the normalized gene expression values from 100 randomly selected cells from each indicated cell identity, and genes displayed are AP-1 targets showing reduced expression by at least 20% in the FFJ KO (Cre^+) and whose expression is detected in at least 25% of analysed nuclei.

CUT&RUN

Hippocampal nuclei from $CaMK2a^{Cre}$/+; LSL-Sun1-sfGFP-Myc/+ mice injected with saline or kainic acid were isolated 2–3 h later as described above. Isolated nuclei were diluted twofold with CUT&RUN wash buffer supplemented with 4 mM EDTA and stained with DRAQ5 (Abcam ab108410) at a 1:500 dilution. $CaMK2a^+$ (GFP^+) nuclei, resulting from CaMK2a–Cre-mediated expression of SUN1-sfGFP-MYC, were isolated by flow cytometry using a Sony SH800Z Cell Sorter and subsequently analysed using FlowJo (10.6). Sorted nuclei were resuspended in 1 ml cold CUT&RUN wash buffer (20 mM HEPES pH 7.5, 150 mM NaCl, 0.2% Tween-20, 1 mg ml^{-1} BSA, 10 mM sodium butyrate and 0.5 mM spermidine supplemented with protease inhibitors), using 50,000 nuclei for each reaction. Nuclei were bound to magnetic concanavalin-A (ConA) beads (Bangs Laboratories) that had been washed with CUT&RUN binding buffer (20 mM HEPES-KOH pH 7.9, 10 mM KCl, 1 mM $CaCl_2$, 1 mM $MnCl_2$). ConA-bead-bound nuclei were then incubated overnight in cold CUT&RUN antibody buffer (CUT&RUN wash buffer supplemented with 0.1% Triton X-100 and 2 mM EDTA) and an in-house rabbit polyclonal anti-FOS antibody (affinity eluted 1096, 1:100) or rabbit IgG antibody (Cell Signaling Technology 2729, 1:100).

After antibody incubation, ConA-bead-bound nuclei were washed with CUT&RUN antibody buffer, resuspended in CUT&RUN Triton-wash buffer (CUT&RUN wash buffer supplemented with 0.1% Triton X-100), and Protein-A-MNase was added at a final concentration of 700 ng ml^{-1}. Samples were incubated at 4 °C for 1 h. The ConA-bead-bound nuclei were then washed twice with CUT&RUN Triton-wash buffer and ultimately resuspended in 100 µl of CUT&RUN Triton-wash buffer. Three microlitres of 100 mM $CaCl_2$ was added to each sample, and samples were incubated on ice for 30 min. The reaction was stopped by the addition of 100 µl of 2× STOP buffer (340 mM NaCl, 20 mM EDTA, 4 mM EGTA, 0.04% Triton X-100, 20 pg ml^{-1} yeast spike-in DNA, and 0.1 µg ml^{-1} RNase A) and incubation at 37 °C for 20 min. After incubation, ConA beads were captured using a magnet, and supernatants containing DNA fragments released by protein-A-MNase were collected. Supernatants were then treated with 2 µl of 10% SDS and 2 µl of 20 mg ml^{-1} proteinase-K and incubated at 65 °C with gentle shaking for 1 h. DNA was then purified using standard phenol/chloroform extraction with ethanol precipitation. DNA was resuspended in 30 µl of 0.1× TE buffer. CUT&RUN sequencing libraries were generated essentially as previously described[41], with the following modifications: Adaptor ligation to end-repaired, and A-tailed DNA was performed using Rapid T4 DNA ligase (Enzymatics). PCR-amplified libraries were purified from adaptor dimers using a 1.1× ratio of AMPure XP beads, eluting in 20 µl of 10 mM Tris pH 8.0. All CUT&RUN libraries were sequenced on Illumina NextSeq 500 (Basespace) using paired-end 40-bp reads.

Analysis. After demultiplexing, sequencing reads were trimmed for quality and remaining adaptor sequence using Trimmomatic v0.36 and kseq. Trimmed reads were aligned to the mm10 genome using Bowtie2 v2.2.9 with the following parameters: –local –very-sensitive-local –no-unal –dovetail –no-mixed –no-discordant –phred33 -I 10 -X 700. Trimmed reads were also aligned to the sacCer3 genome with the same parameters to recover reads corresponding to yeast spike-in DNA used in CUT&RUN. Genome-wide coverage of CUT&RUN fragments was generated using Bedtools v2.27.1 genomecov, normalizing to the number of yeast spike-in reads obtained for each sample. Normalized coverage tracks were visualized using IGV v2.4.10 and represent the average signal across all three biological replicates. CUT&RUN coverage over 100-bp bins genome-wide was determined using Deeptools v3.0.2 multiBigwigSummary and was used to calculate Pearson correlation between pairs of replicate samples for each antibody and stimulus condition. Peaks were identified for FOS CUT&RUN using SEACR v1.1 using the following parameters: norm, relaxed. CUT&RUN performed using rabbit IgG was used as the negative control sample for peak calling. Peaks were subsequently filtered to identify peaks found in all three biological replicates for each condition, creating a conservative set of FOS-bound sites. Peaks within 150 bp of each other were then merged using Bedtools v2.27.1 merge. Plots of spike-in normalized CUT&RUN coverage over peaks were generated by first centering peaks on the maximum of CUT&RUN signal within the peak. CUT&RUN coverage over 50-bp bins spanning 1,000 bp upstream and downstream of the peak centre was calculated using Deeptools v3.0.2 computeMatrix. Coverage in each bin was averaged across all peaks, and average per-bin coverage was plotted in R using ggplot2.

To determine distances between TSS and FOS-binding sites, positions of TSS for Refseq, activity-regulated (CaMK2a-Ribotag), and CA1 excitatory neuron-specific AP-1-regulated (FFJ snRNA-seq) genes were obtained from the UCSC table browser. Distances between FOS-binding sites and the nearest TSS[42] were calculated using Bedtools v2.27.1 closest. Histograms of distances between FOS-bound sites and TSS were plotted in R using ggplot2. We determined the statistical significance of the differences between the distributions of distances for Refseq, CaMK2a–Ribotag, and FFJ snRNA-seq genes using a Wilcoxon rank-sum test in R.

To identify enriched transcription factor motifs within FOS-binding sites, genomic sequences 250 bp upstream and downstream of FOS peak centres were retrieved using Bedtools v2.27.1 getfasta and used as input to MEME-ChIP. Motifs were searched against the HOCOMOCO Mouse v11 CORE database, allowing for multiple occurrences of motifs per sequence and using default settings for all other parameters. The three motifs with the lowest E-value were reported.

NE snRNA-seq

C57BL/6J mice were exposed to a brief 5-min NE stimulus and subsequently returned to their home cages for 1 h or 6 h before hippocampal tissue collection. Nuclei were isolated from hippocampal tissue as described above, and snRNA-seq was performed using the 10X Genomics or inDrops[43] platform. A total of 23,610 nuclei, with a range of 700–15,000 RNA molecule counts per cell and 200–2,500 unique genes per cell, were clustered into ~13 cell types using the UMAP algorithm. The genes *Slc17a7*, *Fibcd1* and *Pex5l* were used as a guide to assign cell type identity to the dorsal CA1 excitatory neuron cluster. Raw UMI counts for each gene were normalized to total UMI counts per cell. Differential gene expression and statistical significance were measured using the Wilcoxon rank-sum test. A down-sampled total of 1,659 CA1 excitatory nuclei were used per condition.

Immunoblotting

Whole-cell extracts from 293T cells were generated by rapid lysis of cells in boiling Laemmli SDS lysis buffer (4% SDS, 20% glycerol, 10% 2-mercaptoethanol, 0.004% bromophenol blue, 0.125 M Tris HCl pH 6.8). Protein extracts were resolved on 4–12% Bis-Tris gradient (Extended Data Fig. 7c) or 8% Tris-Glycine gels (Extended Data Fig. 9g) and subsequently transferred onto nitrocellulose membranes. Membranes were incubated overnight in the following primary antibodies: mouse anti-MYC (Developmental Studies Hybridoma Bank 9E10 in Extended Data Fig. 7c, 1:1,000) or mouse anti-HA (Sigma HA-7, H3663 in Extended Data Fig. 9g, 1:1,000) and rabbit anti-GAPDH (Sigma G9545, 1:2,000). Following washes, membranes were incubated with secondary antibodies conjugated to IRDye 800CW (LI-COR; mouse (926-32210), rabbit (926-32211), 1:5,000) for imaging with the LI-COR Odyssey system.

In vivo silicon probe recordings

For all in vivo electrophysiology recordings, 8–10-week-old *Scg2*$^{fl/fl}$ mice underwent two stereotaxic surgeries. In the first surgery, AAV-Cre-GFP or AAV-ΔCre-GFP was injected into the CA1, and future silicon probe sites over CA1 (Kopf Model 1900; stereotaxic coordinates approximately AP -2 mm and ML ±1.8 mm from bregma) were marked on the surface of the skull. Metabond (Parkell) was used to attach a titanium headplate and cover the remaining exposed skull. Mice were given injections of dexamethasone and buprenorphine SR, and allowed to recover for 1–2 weeks, during which they were exposed to NEs daily and habituated to head-fixation on the air-supported Styrofoam ball. On the day of recording, a second surgery (craniotomy) was performed at one of the marked locations on either the left or right hemisphere. The craniotomy was covered with Kwik-Sil (World Precision Instruments), and the mouse was allowed to recover fully from anaesthesia for at least 4 h. 64-channel silicon probes (Neuronexus) were inserted into the cortex and slowly lowered ~1.25–1.5 mm below the surface of the pia to the pyramidal layer of CA1. In some cases, melted agarose (2% w/v) was applied to the head-plate well to stabilize the probe. Probe advancement was stopped in the pyramidal layer of CA1, as evidenced by the presence of theta oscillations and appearance of multiple units in high density across multiple channels. All data were digitized and acquired at 20 kHz (Intan Technologies RHD2000 Recording system).

Analysis. All data analysis[44] was carried out with custom MATLAB scripts. Channels that were outside of CA1 were excluded from analysis.

Spike sorting was performed using Kilosort2[45] (https://github.com/MouseLand/Kilosort2), followed by manual inspection and curation of clustering using Phy2[46] (https://github.com/cortex-lab/phy). Only well-isolated units were chosen for further analysis. Additionally, single units had to meet the following criteria: detected on fewer than 20 channels, half-maximum spike width of less than 1 ms, at least 1,000 spikes detected in the session, and overall firing rate of > 0.01 spikes s^{-1}. Units were divided into putative excitatory and inhibitory subclasses based on the spike trough to peak duration, as described previously[47], using a cutoff of 0.7 ms, below which units were labelled as inhibitory INs. Due to the low number of inhibitory INs recorded, these were excluded from analyses. For local field potential (LFP) analysis, data from each channel was filtered and downsampled to 1,000 Hz. For theta phase-locking analysis, only periods during running were used in the analysis. A single channel within the stratum pyramidale was chosen as the reference. LFPs were filtered and the Hilbert transform was used to determine the phase. The preferred phase of each neuron was computed as the circular mean of the phase at each spike using the CircStats toolbox in MATLAB[48]. For comparison of single cell properties in the WT and KO groups, cells were pooled across mice. Power spectra were computed between 1 and 120 Hz using the multitaper method (timebandwidth = 5, tapers = 3) in the Chronux toolbox[49]. Power at frequencies between 58–62 Hz were excluded from all subsequent analyses due to 59–61 Hz notch filtering applied (second-order Butterworth filter) to remove noise. Power spectra were computed for each channel individually and averaged across channels. To compare across mice and sessions, individual session power spectra were normalized by the sum over all frequencies in the power spectra (1–120 Hz range). Fraction of spikes as a function of theta phase was computed on an individual unit basis by summing spikes in each 10° bin during running and then dividing by the sum of spikes across all bins.

Reporting summary

Further information on research design is available in the Nature Research Reporting Summary linked to this paper.

Data availability

Ribotag, FFJ snRNA-seq and CUT&RUN data are deposited into the public repository Gene Expression Omnibus (GEO) with accession number GSE158843. All other data will be shared upon reasonable request.

Code availability

Custom code will be provided upon reasonable request.

33. Miyoshi, G. et al. Genetic fate mapping reveals that the caudal ganglionic eminence produces a large and diverse population of superficial cortical interneurons. *J. Neurosci.* **30**, 1582–1594 (2010).
34. Kenner, L. et al. Mice lacking JunB are osteopenic due to cell-autonomous osteoblast and osteoclast defects. *J. Cell Biol.* **164**, 613–623 (2004).
35. Sharma, N. et al. ARNT2 tunes activity-dependent gene expression through NCoR2-mediated repression and NPAS4-mediated activation. *Neuron* **102**, 390–406 (2019).
36. Lin, Y. et al. Activity-dependent regulation of inhibitory synapse development by Npas4. *Nature* **455**, 1198–1204 (2008).
37. Ataman, B. et al. Evolution of Osteocrin as an activity-regulated factor in the primate brain. *Nature* **539**, 242–247 (2016).
38. Mardinly, A. R. et al. Sensory experience regulates cortical inhibition by inducing IGF1 in VIP neurons. *Nature* **531**, 371–375 (2016).
39. Habib, N. et al. Div-Seq: Single-nucleus RNA-seq reveals dynamics of rare adult newborn neurons. *Science* **353**, 925–928 (2016).
40. Cembrowski, M. S., Wang, L., Sugino, K., Shields, B. C. & Spruston, N. Hipposeq: a comprehensive RNA-seq database of gene expression in hippocampal principal neurons. *eLife* **5**, e14997 (2016).
41. Hainer, S. J. & Fazzio, T. G. High-resolution chromatin profiling using CUT&RUN. *Curr. Protoc. Mol. Biol.* **126**, e85 (2019).
42. Malik, A. N. et al. Genome-wide identification and characterization of functional neuronal activity-dependent enhancers. *Nat. Neurosci.* **17**, 1330–1339 (2014).
43. Klein, A. M. et al. Droplet barcoding for single-cell transcriptomics applied to embryonic stem cells. *Cell* **161**, 1187–1201 (2015).
44. Yatsenko, D. et al. DataJoint: managing big scientific data using MATLAB or Python. Preprint at *bioRxiv* https://doi.org/10.1101/031658 (2015).
45. Pachitariu, M., Steinmetz, N., Kadir, S., Carandini, M. & Harris, K. D. Kilosort: realtime spike-sorting for extracellular electrophysiology with hundreds of channels. Preprint at *bioRxiv* https://doi.org/10.1101/061481 (2016).
46. Rossant, C. et al. Spike sorting for large, dense electrode arrays. *Nat. Neurosci.* **19**, 634–641 (2016).
47. Barthó, P. et al. Characterization of neocortical principal cells and interneurons by network interactions and extracellular features. *J. Neurophysiol.* **92**, 600–608 (2004).
48. Berens, P. CircStat: a MATLAB toolbox for circular statistics. *J. Stat. Softw.* **31**, (2009).
49. Bokil, H., Andrews, P., Kulkarni, J. E., Mehta, S. & Mitra, P. P. Chronux: a platform for analyzing neural signals. *J. Neurosci. Methods* **192**, 146–151 (2010).

Acknowledgements We thank all members of the Greenberg laboratory for discussions and critical feedback during the course of this work; all members of the Harvey laboratory for discussions and critical feedback; W. Regehr, D. Ginty, R. Wilson, C. Tzeng, J. Green, E. Pollina and T. Vierbuchen for feedback and critical evaluation of the data and/or manuscript; G. Fishell for the Dlx5/6^{Flp} mice; L. Wu and the Harvard Genome Modification Facility for aiding in the generation of the *Scg2*$^{fl/fl}$ mice; C. Wang and the Boston Children's Hospital Viral Core for generation of AAVs; the Harvard Neurobiology Imaging Facility (NINDS P30 Core Center grant NS072030) for imaging support; and O. Mazor and P. Gorelik at the Harvard Research Instrumentation Core for technical design and support. This work was supported by NIH grants R01 NS028829 and R01 NS115965 (M.E.G.), NIH grant R01 NS089521 (C.D.H.), T32 NS007473 (C.P.D.), F32 NS112455 (C.P.D.), Stuart H.Q. and Victoria Quan fellowship (E-L.Y. and N.L.P.), Harvard Department of Neurobiology graduate fellowship (E.-L.Y.), and Aramont Fund for Emerging Science Research fellowship (E.-L.Y). In addition the Greenberg laboratory is supported by the Allen Discovery Center program, a Paul G. Allen Frontiers Group advised program of the Paul G. Allen Family Foundation.

Author contributions E.-L.Y. and M.E.G. conceived and designed the project. E.-L.Y. designed, executed and analysed all ex vivo electrophysiology, molecular biology, FFJ snRNA-seq and Ribotag experiments with input on all aspects from M.E.G., S.R. and E.C.G. E.-L. Y. designed and validated strategy for generation of *Scg2*$^{fl/fl}$. E.-L.Y., N.L.P., C.D.H. and M.E.G. conceived and designed, E.-L.Y. and N.L.P. executed, and N.L.P. analysed in vivo silicon probe recordings. E.-L.Y. and C.P.D. designed and executed, and C.P.D. analysed CUT&RUN. M.A.N. and N.S. assisted in analysis of FFJ snRNA-seq. D.A.H. analysed Ribotag sequencing. E.-L.Y., E.G. and N.L.P. executed and analysed Morris water maze experiments. O.D. designed, executed and analysed NE snRNA-seq. C.L. and N.S. assisted in molecular biology. E.-L.Y. and M.E.G. wrote the manuscript with input from all authors.

Competing interests The authors declare no competing interests.

Additional information

Supplementary information is available for this paper at https://doi.org/10.1038/s41586-020-3031-0.

Correspondence and requests for materials should be addressed to M.E.G.

Peer review information *Nature* thanks Hyung-Bae Kwon, Elly Nedivi and Thomas Sudhof for their contribution to the peer review of this work.

Reprints and permissions information is available at http://www.nature.com/reprints.

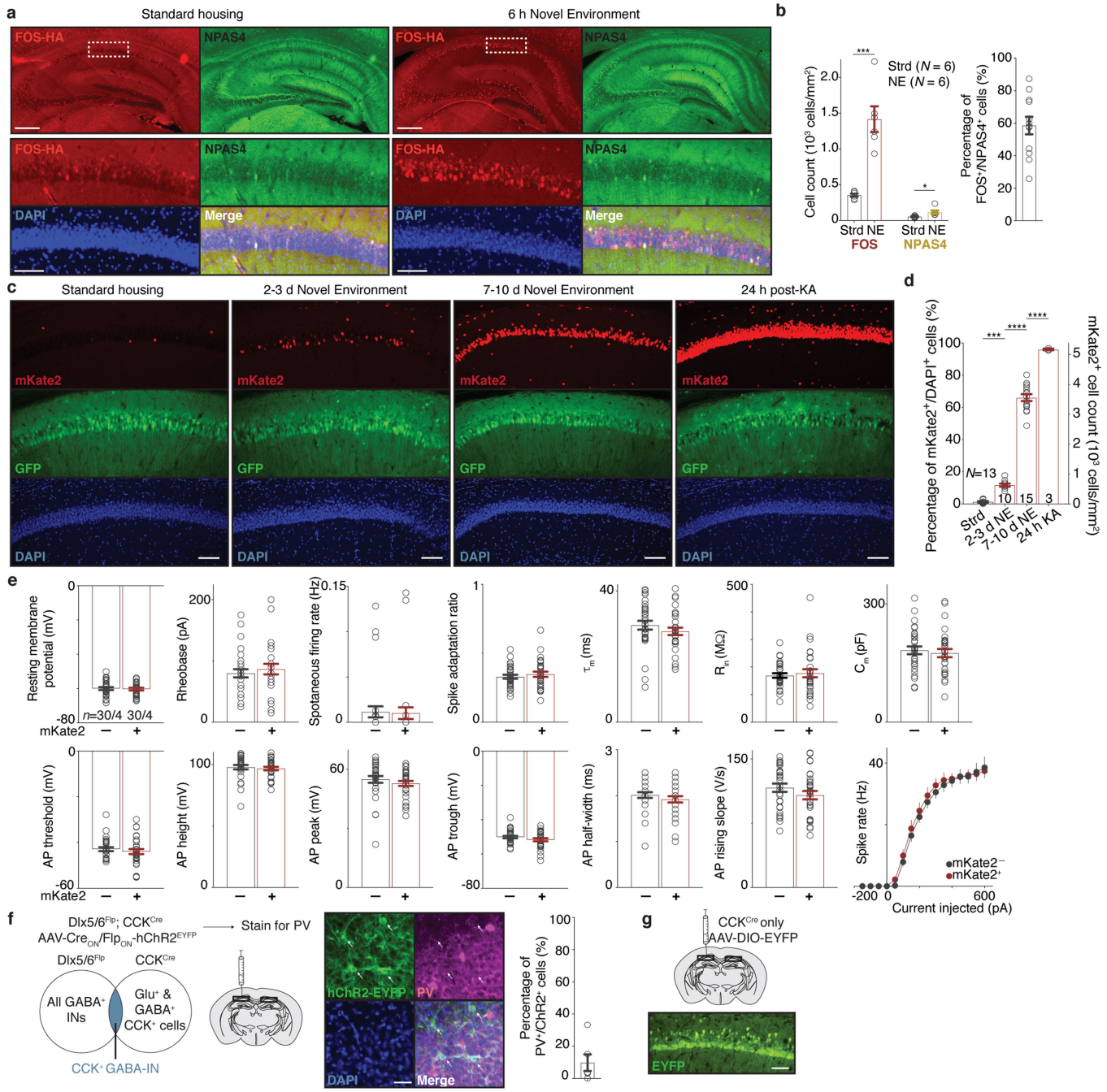

Extended Data Fig. 1 | See next page for caption.

Extended Data Fig. 1 | Characterization of novel environment paradigm, AAV-based mKate2 activity reporter, and intersectional genetic strategy for CCK-INs. a, Top, representative immunostaining images of FOS and NPAS4 in hippocampus obtained from mice housed under standard (Strd) conditions (left) or exposed to NE (right) for 6 h. Scale, 400 µm. Bottom, higher magnification of insets. Scale, 100 µm. To immunostain for both FOS and NPAS4 proteins in the same sections, mice where FOS or NPAS4 had been endogenously tagged with a Flag-HA tag (*Fos*-FlagHA[19] or *Npas4*-FlagHA[35]) were used with a rat anti-HA antibody, while the reciprocal protein was probed with a rabbit polyclonal antibody (Methods). **b**, Left, number of FOS^+ and $NPAS4^+$ nuclei in the CA1 of standard or 6 h NE mice. Strd, $N = 6$ mice; NE, $N = 6$ mice. Note that within CA1, significantly fewer $NPAS4^+$ cells were detected, indicating that the AAV-based mKate2 activity reporter mainly labels *Fos*-activated neurons. Two-sided *t*-test, $^{***}P = 1.6 \times 10^{-4}$, $^{*}P = 0.033$. Right, quantification of number of $NPAS4^+$ cells that are also FOS^+. **c**, Representative images of $mKate2^+$ neurons across different time points and conditions as in **d**. An AAV encoding GFP was used as a control for the viral injections. Scale, 100 µm. **d**, Percentages of $mKate2^+$ neurons over total number of $DAPI^+$ cells (left *y*-axis) or density of $mKate2^+$ neurons (right *y*-axis). The average percentages of $mKate2^+$ neurons are 1%, 12%, 66% and 96% under Strd ($N = 13$ mice), 2-3 d NE ($N = 10$ mice, $^{***}P = 2.7 \times 10^{-4}$), 7-10 d NE ($N = 15$ mice, $^{****}P < 1 \times 10^{-15}$), and 24 h post-KA injection ($N = 3$ mice, $^{****}P = 7.3 \times 10^{-10}$), respectively. Ordinary one-way ANOVA, with multiple comparisons correction. Note that data for Strd and 2-3 d NE are replotted from Fig. 1c. **e**, Bar plots of additional electrophysiological parameters for $mKate2^-$ and $mKate2^+$ neurons. $n = 30$ pairs/4 mice per group. Two-sided *t*-test, not significant (n.s.) for all parameters. **f**, Left, schematic of intersectional genetic strategy involving $Dlx5/6^{Flp}$;CCK^{Cre} mice transduced with a dual Cre/Flp recombinase-dependent $ChR2^{EYFP}$ fusion protein necessary to specifically target CCK-INs. Middle, representative immunostaining for PV in magenta; $ChR2^{EYFP}$ in green. Right, percentage of $ChR2^+$ cells in the CA1 field showing overlap with PV expression is low, indicating that the $Dlx5/6^{Flp}$;CCK^{Cre} line is suited for genetic targeting of CCK-INs. $N = 4$ mice. Scale, 40 µm. **g**, Representative image of CA1 region of CCK^{Cre} mice transduced with AAV encoding Cre-dependent EYFP depicting widespread EYFP expression in the CA1 and underscoring the necessity of the intersectional strategy in **f** for targeting CCK-INs specifically. $N = 2$ mice. Scale, 100 µm. In **b**, **d**–**f**, data are mean ± s.e.m. In **f**, **g**, schematic images were adapted with permission from Paxinos & Franklin (ref. [32]).

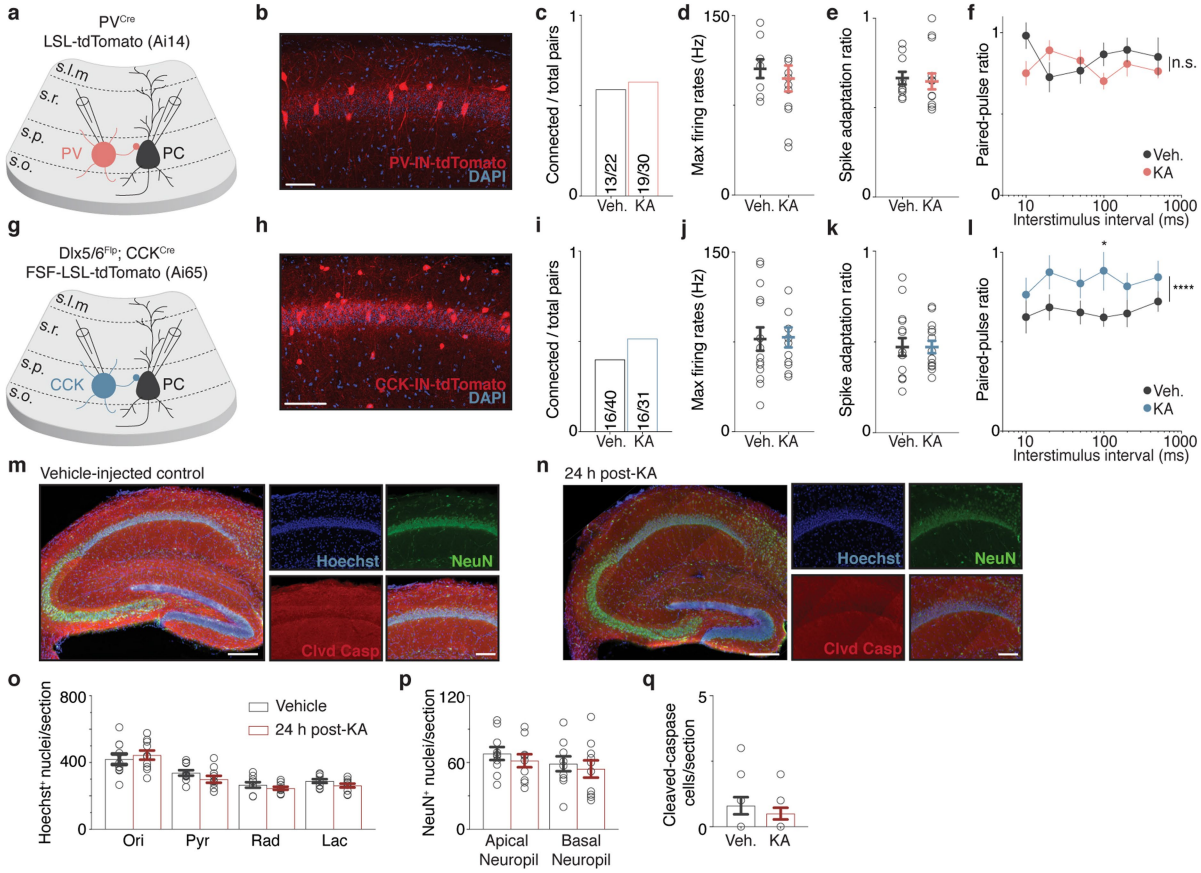

Extended Data Fig. 2 | IN-to-CA1 PC paired recordings and cell health parameters in 24 h post-KA condition. a, **g**, Schematic of genetic strategy to label PV-INs (PV^{Cre};Ai14) or CCK-INs (Dlx5/6^{Flp};CCK^{Cre};Ai65). **b**, **h**, Representative images of tdTomato fluorescence in the CA1 field. Scale, 100 µm. $N = 2$ mice per line. **c**, **i**, Quantification of the fraction of (**c**) PV- or (**i**) CCK-to-CA1 PC synaptically-connected pairs from the overall number of pairs recorded in both vehicle (Veh.) and 24 h post-KA mice. (**c**) Veh., $n = 13/22$; KA, $n = 19/30$; (**i**) Veh., $n = 16/40$; KA, $n = 16/3$, where n = number of connections/total pairs. **d**, **j**, Quantification of maximum firing rate of (**d**) PV- or (**j**) CCK-INs from connected pairs. (**d**) Veh., $n = 10/6$; KA, $n = 14/7$; (**j**) Veh., $n = 15/9$; KA, $n = 14/4$, where n = number of cells/number of mice. **e**, **k**, Quantification of spike adaptation ratio of (**e**) PV- or (**j**) CCK-INs from connected pairs as in **d**, **j**. **f**, **l**, Quantification of paired pulse ratios (PPRs) of uIPSCs at the indicated interstimulus intervals (ISI) for (**f**) PV- (Veh., $n = 13/6$; KA, $n = 19/7$) or (**l**) CCK- (Veh., $n = 16/9$; KA, $n = 16/4$) to-CA1 PC connected pairs, where n = number of pairs/number of mice. Two-sided t-tests performed at each ISI or for all ISIs comparing Veh. and 24 h post-KA conditions; $^{*}P = 0.039$, $^{****}P = 4.4 \times 10^{-5}$. **m**, **n**, Representative hippocampal images from (**m**) Veh. and (**n**) 24 h post-KA conditions. Sections were immunostained for NeuN (green) and cleaved-caspase 3 (red), and counterstained with Hoechst (blue). Scale, 200 µm (left); 100 µm (right, CA1 field). $N = 2$ mice per condition. **o**–**q**, Quantification of (**o**) Hoechst^{+} nuclei, (**p**) NeuN^{+} nuclei, and (**q**) cleaved-caspase^{+} cells per 40-µm section in all layers of CA1. Ori, stratum oriens; Pyr, stratum pyramidale; Rad, stratum radiatum; Lac, stratum lacunosum moleculare. Results suggest that KA injection does not induce cell death within 24 h. Veh. and KA, $n = 10$ sections/2 mice, respectively. In **d**–**f**, **j**–**l**, **o**–**q**, data are mean ± s.e.m.

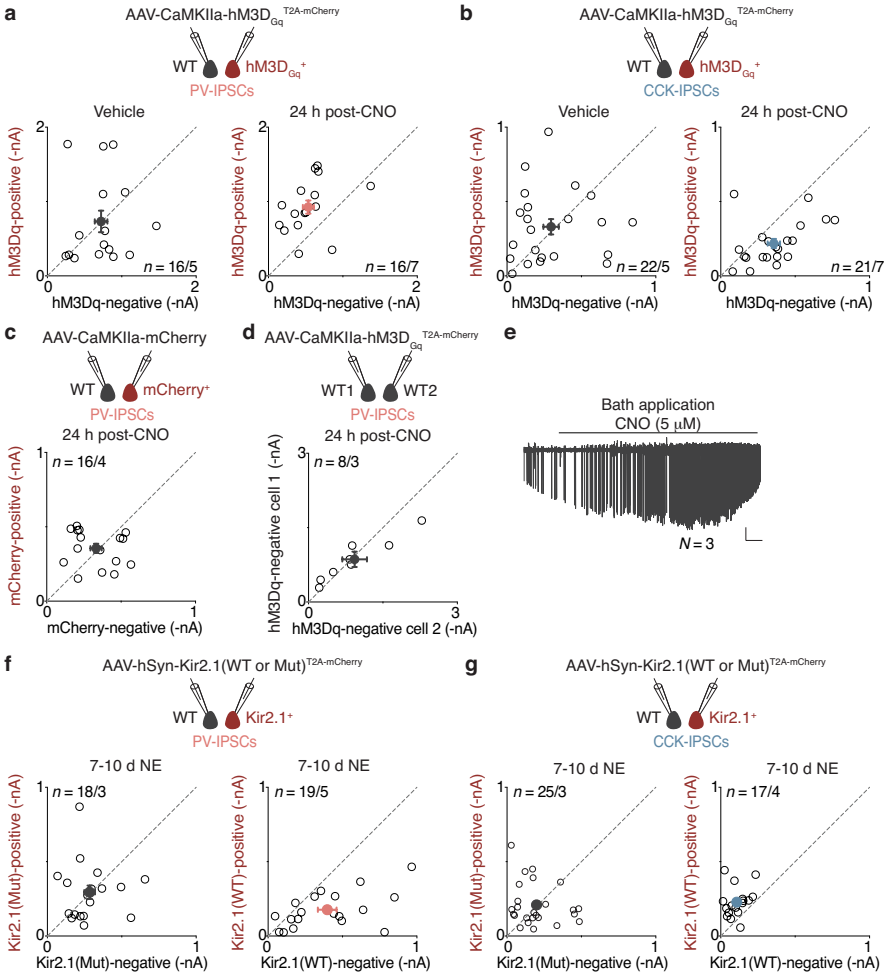

Extended Data Fig. 3 | Chemogenetic activation of CA1 PCs recapitulated bidirectional changes in perisomatic inhibition while silencing of CA1 PCs led to inverse effects. a–**d**, **f**, **g**, Top, schematic of recording configuration. Bottom, scatter plots of (**a**, **c**, **d**, **f**) PV- or (**b**, **g**) CCK-IPSCs recorded from untransduced WT and indicated viral-transduced neighbouring CA1 PCs. (**a**) Veh., $n = 16/5$; CNO, $n = 16/7$; (**b**) Veh., $n = 22/5$; CNO, $n = 21/7$; (**c**) CNO, $n = 16/4$; (**d**) Note: pairs of untransduced cells, CNO, $n = 8/3$; (**f**) KirMut, $n = 18/3$; Kir2.1, $n = 19/5$; (**g**) KirMut, $n = 25/3$; Kir2.1, $n = 17/4$, where n = number of pairs/number of mice and each open circle represents a pair of simultaneously recorded neurons, with closed circles representing mean ± s.e.m. **e**, Representative trace of spikes detected from a CA1 PC in cell-attached mode in slice after bath application of CNO. As expected, addition of CNO led to firing rate increases in hM3D$_{Gq}$-expressing neurons, providing further confidence that intraperitoneal CNO injection in mice in vivo chemogenetically activates hM3D$_{Gq}$-expressing neurons in the CA1. $N = 3$ cells/3 mice. Scale, 50 pA, 60 s.

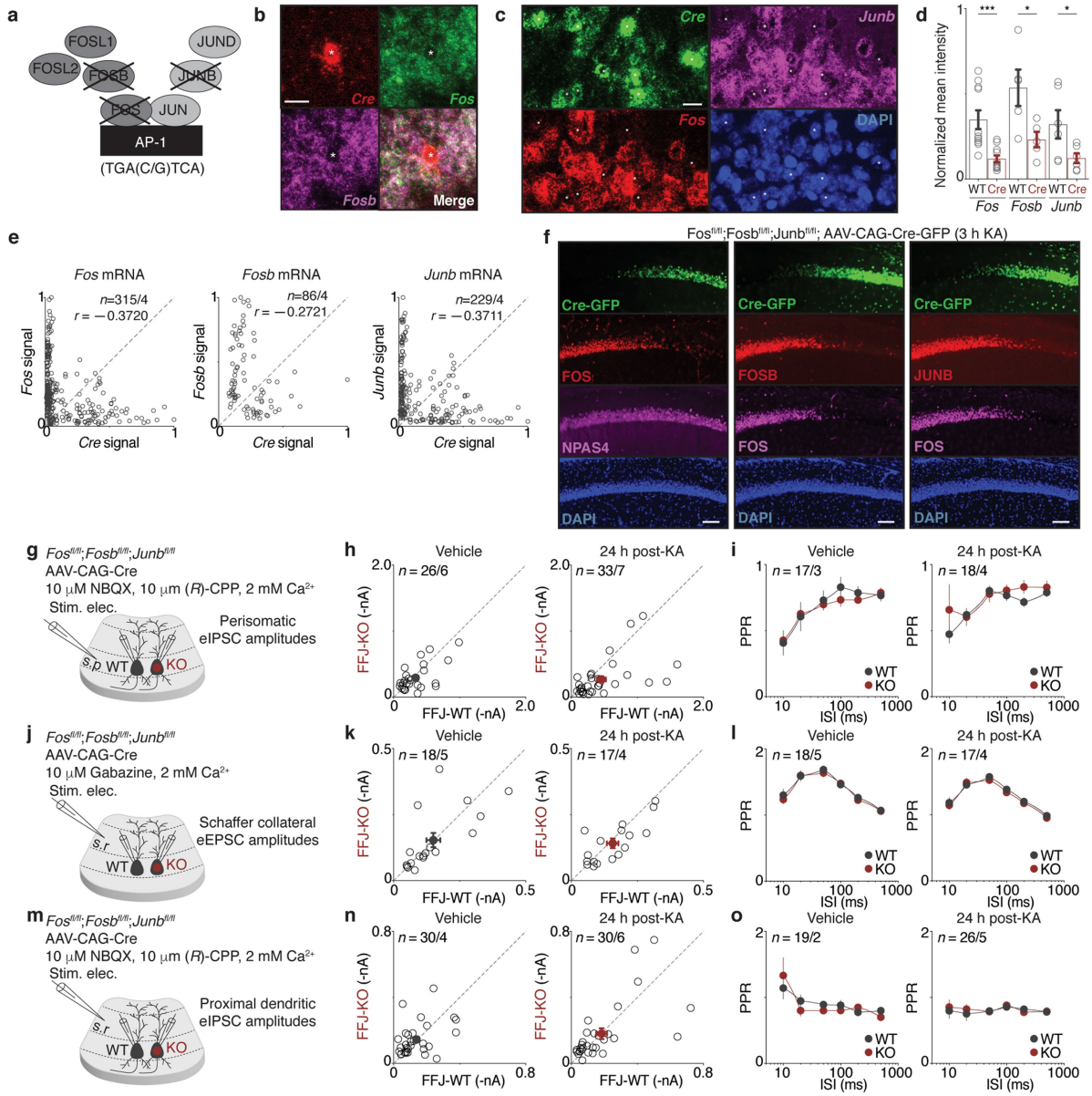

Extended Data Fig. 4 | Validation of *Fos*$^{fl/fl}$;*Fosb*$^{fl/fl}$;*Junb*$^{fl/fl}$ (FFJ) mouse line and additional electrophysiological parameters in FFJ-WT and KO cells. **a**, Schematic representation of the AP-1 members conditionally deleted in FFJ line. **b**, **c**, Representative images of smRNA-FISH validating loss of *Fos* and *Fosb* (and *Junb* in **c**) upon *Cre* expression in the CA1 field of 1-1.5 h post-KA-injected FFJ mice. Scale, 20 μm. $N = 4$ mice. **d**, Normalized pixel intensity for Cre-negative and Cre-positive cells. Each point represents the average for individual sections across $N = 4$ mice. Two-sided *t*-tests, *Fos*, $^{***}P = 7.7 \times 10^{-4}$; *Fosb*, $^{*}P = 0.031$; *Junb*, $^{*}P = 0.047$. **e**, Scatter plots of normalized pixel intensities of *Cre* signal against *Fos*, *Fosb* or *Junb* signals for each cell. Pearson correlation coefficients (*r*) shown. *Fos*, $n = 315$; *Fosb*, $n = 86$; *Junb*, $n = 229$ cells from $N = 4$ mice. **f**, Representative images of Cre-injected sections immunostained for FOS, FOSB, JUNB, and NPAS4 proteins in the CA1 field of 3 h post-KA-injected FFJ mice. Scale, 100 μm. $N = 3$ mice. **g**, **j**, **m**, Schematic of stimulus electrode (stim. elec.) placement in stratum pyramidale (s.p.) to stimulate perisomatic inhibitory axons (**g**), or stratum radiatum (s.r.) to stimulate Schaffer collaterals (**j**) or proximal dendritic inhibitory axons (**m**). **h**, **k**, **n**, Scatter plots of recorded pairs of FFJ-WT and FFJ-KO CA1 PCs in 24 h post-vehicle (left) or -KA injected (right) mice, where (**h**) Veh., $n = 26/6$; KA, $n = 33/7$; (**k**) Veh., $n = 18/5$; KA, $n = 17/4$; (**n**) Veh., $n = 30/4$; KA, $n = 30/6$. **i**, **l**, **o**, Quantification of PPRs for indicated currents, where (**i**) Veh., $n = 17/3$; KA, $n = 18/4$; (**l**) Veh., $n = 18/5$; KA, $n = 17/4$; (**o**) Veh., $n = 19/2$; KA, $n = 26/5$. In **h**, **i**, **k**, **l**, **n**, **o**, *n* = number of pairs/number of mice. In **d**, **h**, **i**, **k**, **l**, **n**, **o**, data are mean ± s.e.m.

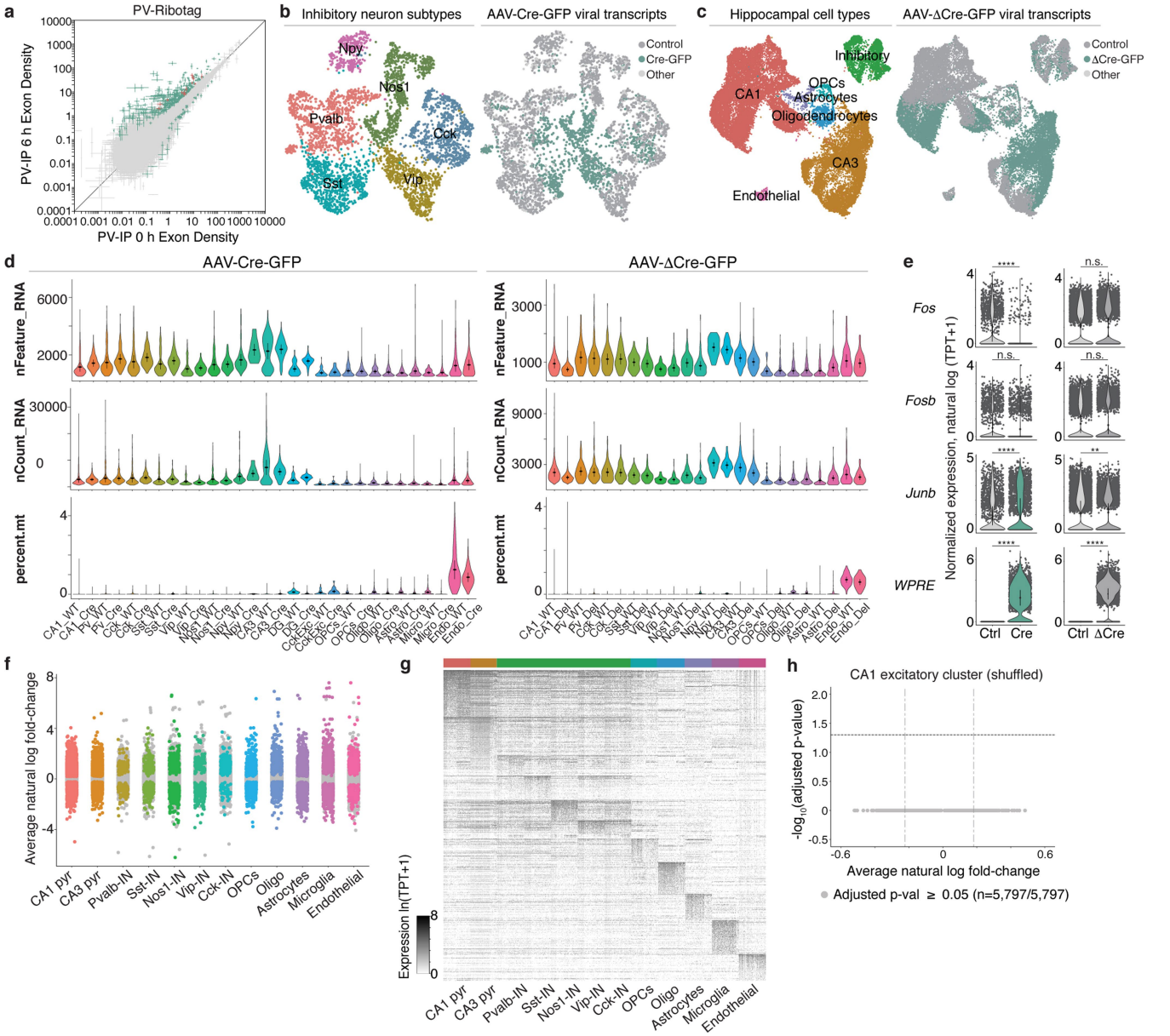

Extended Data Fig. 5 | RNA-sequencing to identify CA1 pyramidal neuron-specific FOS targets. a, Scatter plot showing PV-specific ARGs identified by comparing 6 h post-KA to vehicle-injected conditions. Significantly different genes (green); FDR ≤ 0.005. PV-enriched (IP over input) genes (red). Points represent mean ± s.e.m. n = 9-10 mice per biological replicate; 4 biological replicates per condition. **b**, UMAP visualization of IN subtypes using only *Gad2*-expressing ("Inhibitory") cells from Fig. 3d. **c**, UMAP visualization of ΔCre$^+$ and respective control nuclei with (left) cell type information or (right) genotype assignments overlaid. Control, ΔCre$^-$ in control hemispheres; ΔCre-GFP, ΔCre$^+$ in injected hemispheres; Other, ΔCre$^-$ or ΔCre$^+$ in injected or control hemispheres, respectively. n = 25,214 cells/4 mice. **d**, Quality control metrics for each transcriptionally distinct cell type identified by snRNA-seq in both Cre$^+$ and ΔCre$^+$ ("Del") samples compared with their respective untransduced controls ("WT") as in Fig. 3d and **c**. Top, number of unique genes per cell. Middle, number of RNA molecules per cell. Bottom, percentage of reads that map to mitochondrial genome. CA1, CA1 PCs; Pv, Pvalb$^+$ INs; Cck, Cck$^+$ INs; Sst, Sst$^+$ INs; Vip, Vip$^+$ INs; Nos1, Nos1$^+$ INs; Npy, Npy$^+$ INs; CA3, CA3 excitatory neurons; DG, dentate gyrus neurons; Cck Exc, Cck$^+$ excitatory neurons; OPCs, oligodendrocyte precursor cells; Oligo, oligodendrocytes; Astro, astrocytes; Micro, microglia; Endo, endothelial cells. **e**, Violin plots depicting CA1 PC-specific expression of *Fos* (****$P = 9.7 \times 10^{-127}$), *Fosb*,*Junb* (****$P = 7.2 \times 10^{-26}$; **$P = 0.003$), and viral-derived *WPRE* (****$P = 0$). Ctrl, untransduced control nuclei. Note that the design of the FFJ line renders snRNA-seq validation of excision of *Fosb* and *Junb* suboptimal (see Extended Data Fig. 4b–f and Methods). TPT, tags per ten thousand. **f**, Strip plot displaying differential gene expression between Cre$^+$ and control samples for each transcriptionally distinct cell type. Colored points represent significant genes (Bonferroni-corrected $P < 0.05$, with average natural log fold-change (FC) ≥ 20%); grey points represent non-significant genes. **g**, Heatmap depicting normalized gene expression values from 100 randomly selected cells from each indicated cell type identity. Genes are cell-type-enriched AP-1 targets downregulated by at least 20% with loss of AP-1, and whose expression is detected in at least 25% of untransduced cells. **h**, Volcano plot of shuffled data where Cre$^+$ and control CA1 excitatory nuclei were randomly assigned between two groups, showing no significant gene expression differences (light grey; Bonferroni-corrected $P >$ 0.05), thus further indicating that the expression differences observed between Cre$^+$ and control were due to presence of Cre. Data are mean ± 2 × s.d. (**d**, **e**); two-sided Wilcoxon rank-sum test (**e**–**h**).

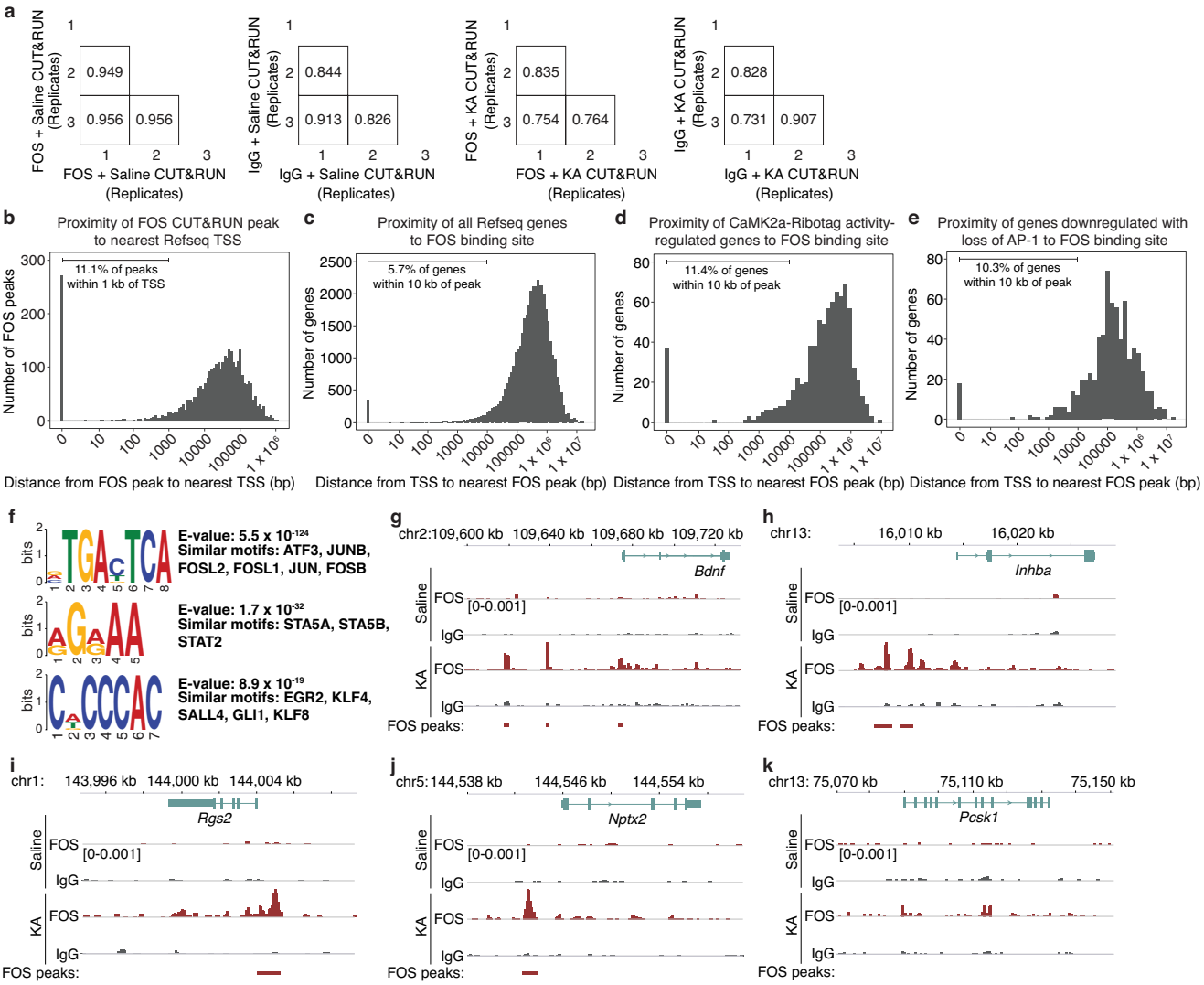

Extended Data Fig. 6 | CaMK2a-SUN1 FOS CUT&RUN revealed FOS binding sites across genome. a, Pairwise Pearson correlation between CaMK2a-SUN1 FOS CUT&RUN biological replicates for each antibody and stimulus condition. **b**, Histogram plotting distribution of distances between CaMK2a-SUN1 FOS CUT&RUN peaks and the nearest Refseq transcription start site (TSS). Peaks with a distance of 0 overlap the TSS. As expected[42], ~90% of FOS-bound sites are distal to the TSS. **c**–**e**, Histograms plotting distributions of distances between the TSS of (**c**) all Refseq genes, (**d**) CaMK2a-Ribotag ARGs, or (**e**) CA1 excitatory genes downregulated with AP-1 loss (FFJ snRNA-seq), and the nearest FOS binding site. A distance of 0 indicates overlap of a FOS peak with the TSS. Notably, both CaMK2a-specific ARGs (**d**) and putative AP-1 targets downregulated with AP-1 loss in FFJ snRNA-seq (**e**) are significantly enriched for FOS-bound sites, which are significantly closer to the TSS when compared to all genes (**c**) ($P < 2.2 \times 10^{-16}$, two-sided Wilcoxon rank-sum test), providing further support that these genes are direct targets of FOS. **f**, Top three enriched motifs identified by MEME-ChIP from CaMK2a-SUN1 FOS CUT&RUN peaks. E-values and matching transcription factor motifs are displayed to the right of each enriched motif. FOS CUT&RUN peaks identified therefore show significant enrichment for the AP-1 motif. **g**–**k**, Tracks displaying FOS or IgG binding under 2-3 h post-vehicle or KA conditions for genomic regions surrounding the (**g**) *Bdnf*, (**h**) *Inhba*, (**i**) *Rgs2*, (**j**) *Nptx2*, or (**k**) *Pcsk1* genes (see Fig. 4i for *Scg2*). *y*-axis shows spike-in normalized CUT&RUN coverage. Tracks are scaled to the maximum value observed for all samples for the displayed genomic locus, shown in brackets.

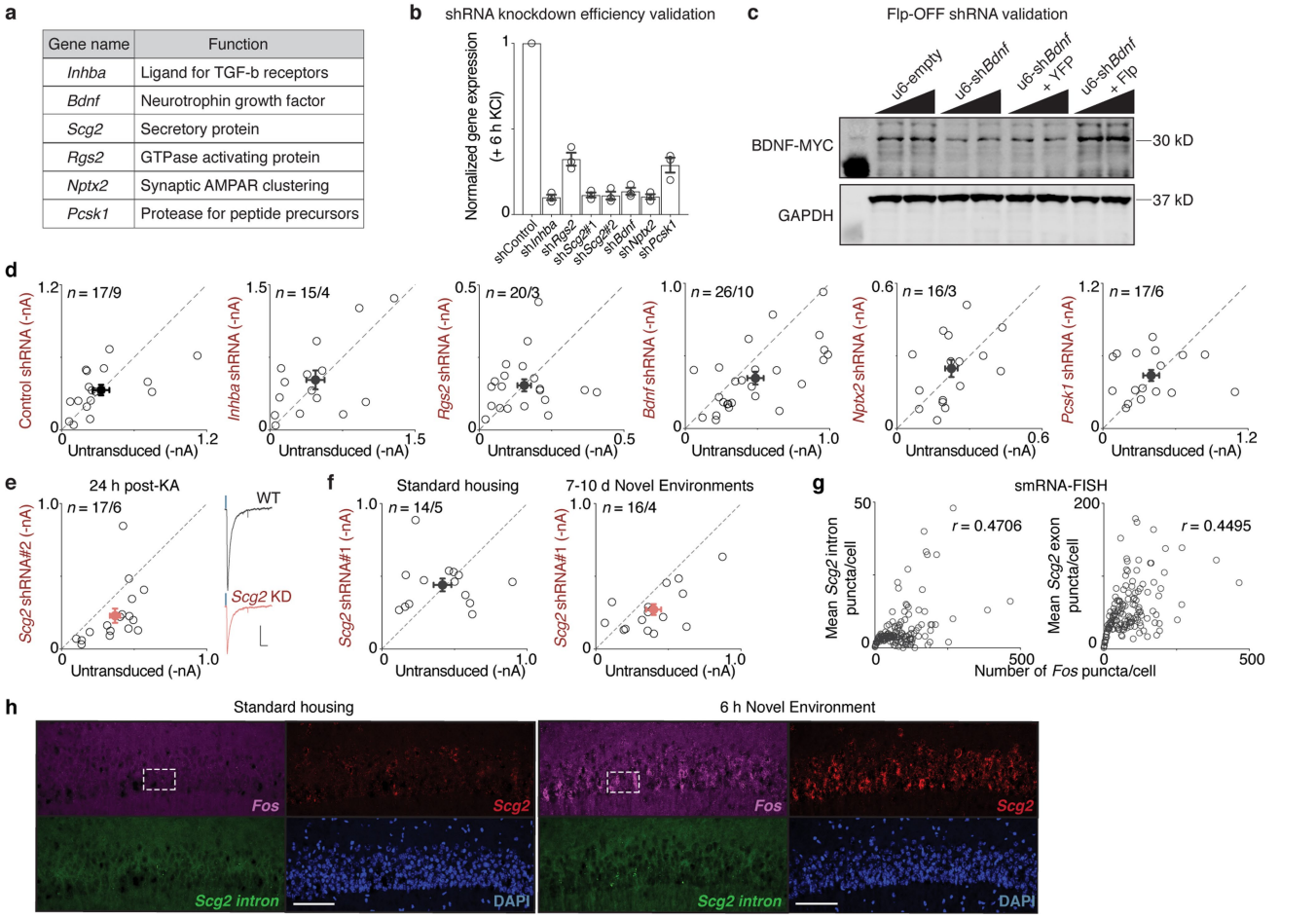

Extended Data Fig. 7 | Analyses of AP-1-regulated candidate genes to identify molecular effector(s) of bidirectional perisomatic inhibitory plasticity. a, Table of high-confidence AP-1-regulated candidate genes analysed and their known functions. **b**, RT–qPCR validation of shRNA efficacy using cultured hippocampal neurons transduced with lentivirus encoding the indicated shRNA. $n = 3$ biological replicates for each shRNA. Data are mean ± s.e.m. **c**, Western blot confirmation of the efficacy of the Flp-OFF shRNA strategy, where *Bdnf* shRNA-containing plasmid was transfected in 293T cells along with BDNF-MYC, and excision of the shRNA expression cassette via introduction of Flp recombinase was confirmed. Loading controls (GAPDH) were run on a separate blot (see Supplementary Fig. 2a for full scans). 100- or 500-ng transfections of indicated u6-plasmid were loaded side-by-side on blot. $n = 2$ biological replicates. **d**–**f**, Scatter plots of recorded PV-IPSC amplitudes from untransduced shRNA$^-$ and neighbouring shRNA$^+$ CA1 PCs from mice 24 h post-KA injection. The shRNA target is shown on the *y*-axis: (**d**) Control, $n = 17/9$; *Inhba*, $n = 15/4$; *Rgs2*, $n = 20/3$; *Bdnf*, $n = 26/10$; *Nptx2*, $n = 16/3$; *Pcsk1*, $n = 17/6$; (**e**) *Scg2* shRNA#2, $n = 17/6$. Representative traces from a pair of neurons shown; blue marks depict light onset. Scale, 100 pA, 40 ms; (**f**) *Scg2* shRNA#1, Strd, $n = 14/5$; 7-10 d NE, $n = 16/4$, where n = number of pairs/number of mice. Each open circle represents a pair of simultaneously recorded neurons; closed circles represent mean ± s.e.m. **g**, smRNA-FISH scatter plots as in Fig. 4k depicting the correlation between *Fos* and (left) *Scg2* intron or (right) *Scg2* mRNA expression. Each point represents the mean number of *Scg2* puncta/cell within a bin, with a bin width of 1 *Fos* punctum/cell. Pearson correlation coefficients (r) are shown. **h**, Lower magnification images of smRNA-FISH as in Fig. 4j. Scale, 100 µm.

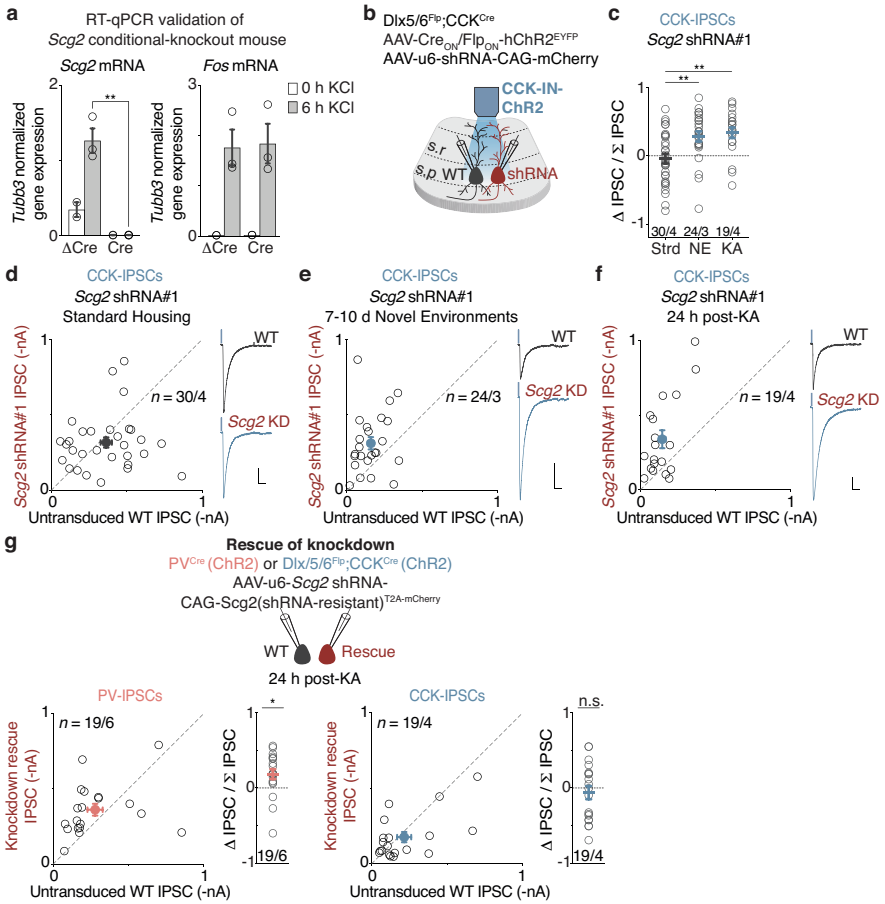

Extended Data Fig. 8 | SCG2 is a molecular effector of bidirectional perisomatic inhibitory plasticity. a, RT–qPCR validation of *Scg2*$^{fl/fl}$ conditional-knockout line, where normalized (left) *Scg2* and (right) *Fos* RNA levels in cultured hippocampal neurons derived from *Scg2*$^{fl/fl}$ mice are shown. Cultures were transduced with lentiviral Cre or ΔCre and membrane depolarized with KCl for 0 h or 6 h. $n = 3$ biological replicates. Data are mean ± s.e.m.; two-sided *t*-test, $^{**}P = 0.002$. **b**, Schematic of intersectional genetic strategy to introduce ChR2 into CCK-INs and sparsely introduce shRNAs specifically into CA1 PCs of Dlx5/6^{Flp};CCK^{Cre} mice. **c**, Normalized differences in CCK-IPSC amplitudes between pairs of *Scg2* shRNA^{-} and shRNA^{+} PCs depicted in **d**–**f**. Strd, $n = 30/4$; NE, $n = 24/3$; KA, $n = 19/4$. Data are mean ± s.e.m. Ordinary one-way ANOVA, with multiple comparisons correction; NE, $^{**}P = 0.005$; KA, $^{**}P = 0.002$. **d**–**f**, Scatter plots of CCK-IPSC amplitudes of pairs as in **c**. Representative traces from pairs of neurons shown; blue marks depict light onset. Scale, 100 pA, 40 ms. **g**, Top, schematic of recording configuration. Scatter plots of (bottom left) PV-IPSC or (bottom right) CCK-IPSC amplitudes recorded from pairs of neurons of which one was untransduced (WT) and the other expressed a *Scg2* shRNA#1 with an shRNA-resistant full-length SCG2 rescue construct. Normalized differences in IPSC amplitudes between pairs of neurons shown to the right of each scatter plot. PV, $n = 19/6$; CCK, $n = 19/4$. Two-sided one-sample *t*-test with hypothetical mean of 0, $^{*}P = 0.011$. In **c**–**g**, each open circle represents a pair of simultaneously recorded neurons; closed circles represent mean ± s.e.m.; *n* = number of pairs/number of mice.

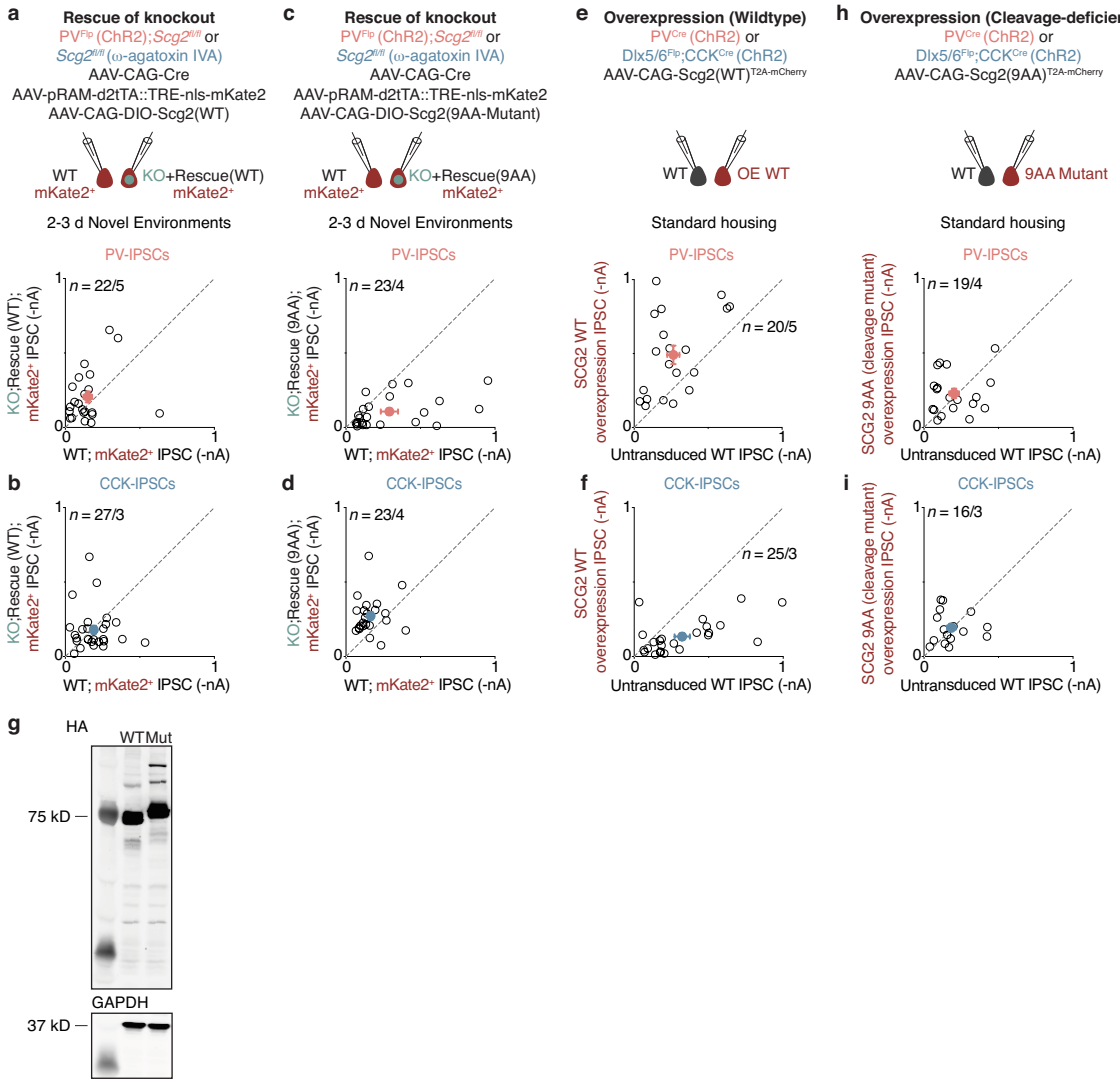

Extended Data Fig. 9 | A series of rescue and overexpression analyses suggest a critical role for the processing of SCG2. a, **b**, Scatter plots of PV-IPSC (**a**) and CCK-IPSC (**b**) amplitudes recorded from mKate2$^+$ pairs that are either Cre$^-$ (WT) or Cre$^+$ (KO). *Scg2*-KO neurons also expressed a Cre-dependent full-length SCG2 construct (Rescue WT) to rescue the loss of *Scg2*. PV, $n = 22/5$; CCK, $n = 27/3$. **c**, **d**, As in **a**, **b** but using a Cre-dependent non-cleavable SCG2 mutant (Rescue 9AA) instead, which failed to rescue the loss of *Scg2*. PV, $n = 23/4$; CCK, $n = 23/4$. **e**, **f**, Scatter plots of PV-IPSC (**e**) and CCK-IPSC (**f**) amplitudes recorded from untransduced (WT) and neighbouring full-length SCG2-overexpressing CA1 PCs (OE WT), showing that gain-of-function of SCG2 is sufficient to induce bidirectional perisomatic inhibitory plasticity in the absence of neural activity. PV, $n = 20/5$; CCK, $n = 25/3$. **g**, Western blot confirmation of stable expression of SCG2 and the non-cleavable SCG2 mutant (9AA-Mutant) constructs containing an HA-tag in 293T cells. Expression levels were measured by immunoblot analysis with HA antibody. Loading controls (GAPDH) were run on a separate blot (see Supplementary Fig. 2b for full scans). $n = 2$ biological replicates. **h**, **i**, As in **e**, **f** but with overexpression of the non-cleavable SCG2 mutant (9AA Mutant) instead, which failed to induce changes in inhibition. PV, $n = 19/4$; CCK, $n = 16/3$. In **a**–**f**, **h**, **i**, each open circle represents a pair of simultaneously recorded neurons; closed circles represent mean ± s.e.m; n = number of pairs/number of mice.

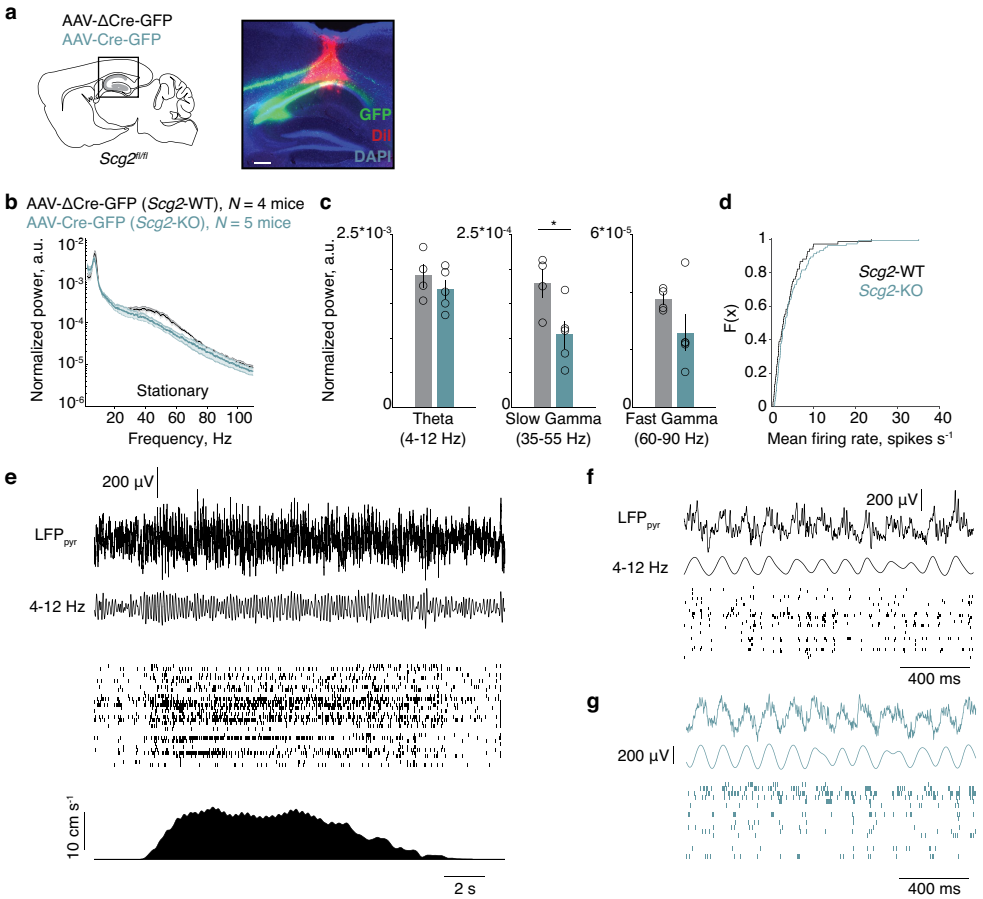

Extended Data Fig. 10 | Silicon probe recordings in *Scg2*-WT and *Scg2*-KO mice to assess effects on network oscillations. a, Left, schematic of stereotaxic injection and recording site in CA1 pyramidal layer. Right, representative image of silicon probe placement in CA1 pyramidal layer with Cre-GFP (green) and DiI (red). $N = 4$ mice. Scale, 200 µm. **b**, Normalized power spectra of network oscillations in *Scg2*-WT or *Scg2*-KO mice during stationary periods. Average across *Scg2*-WT (grey, $N = 4$) or *Scg2*-KO (green, $N = 5$) mice, one session per mouse. Data are mean ± s.e.m. **c,** Mean of the normalized power spectra within theta, slow-gamma, and fast-gamma bands during stationary periods as shown in **b**. Two-sided *t*-test, $^*P = 0.037$. Data are mean ± s.e.m. **d**, Cumulative histogram of mean firing rate for all *Scg2*-WT and *Scg2*-KO units. Mean firing rate is not significantly different (two-sided *t*-test, $P = 0.2138$). *Scg2*-WT ($n = 67$ units) and *Scg2*-KO ($n = 103$ units). **e**, Example local field potential (LFP), single-unit activity, and running speed in a *Scg2*-WT mouse. From top to bottom: Denoised and downsampled LFP, 4-12 Hz bandpass filtered LFP, population spiking activity raster plot, and smoothed running speed. **f**, Expanded snippet of data from the example in **e**. From top to bottom: Denoised and downsampled LFP, 4-12 Hz bandpass filtered LFP, and population spiking activity raster plot. **g**, As in **f** but with example data from a *Scg2*-KO mouse. Schematic image in **a** (left) adapted with permission from Paxinos & Franklin (ref. [32]).

nature research

Corresponding author(s): Michael E. Greenberg

Last updated by author(s): Oct 5, 2020

Reporting Summary

Nature Research wishes to improve the reproducibility of the work that we publish. This form provides structure for consistency and transparency in reporting. For further information on Nature Research policies, see our Editorial Policies and the Editorial Policy Checklist.

Statistics

For all statistical analyses, confirm that the following items are present in the figure legend, table legend, main text, or Methods section.

n/a	Confirmed
☐	☒ The exact sample size (*n*) for each experimental group/condition, given as a discrete number and unit of measurement
☐	☒ A statement on whether measurements were taken from distinct samples or whether the same sample was measured repeatedly
☐	☒ The statistical test(s) used AND whether they are one- or two-sided *Only common tests should be described solely by name; describe more complex techniques in the Methods section.*
☒	☐ A description of all covariates tested
☐	☒ A description of any assumptions or corrections, such as tests of normality and adjustment for multiple comparisons
☐	☒ A full description of the statistical parameters including central tendency (e.g. means) or other basic estimates (e.g. regression coefficient) AND variation (e.g. standard deviation) or associated estimates of uncertainty (e.g. confidence intervals)
☐	☒ For null hypothesis testing, the test statistic (e.g. *F*, *t*, *r*) with confidence intervals, effect sizes, degrees of freedom and *P* value noted *Give P values as exact values whenever suitable.*
☒	☐ For Bayesian analysis, information on the choice of priors and Markov chain Monte Carlo settings
☒	☐ For hierarchical and complex designs, identification of the appropriate level for tests and full reporting of outcomes
☐	☒ Estimates of effect sizes (e.g. Cohen's *d*, Pearson's *r*), indicating how they were calculated

Our web collection on statistics for biologists contains articles on many of the points above.

Software and code

Policy information about availability of computer code

Data collection	For ex vivo electrophysiology, Clampex 10.6 was used. For RNA-sequencing and CUT&RUN, Basespace (Illumina) was used to handle files extracted from NextSeq500 reads. For in vivo electrophysiology, Intan Technologies RHD2000 recording system was used. For images of brain sections, virtual slide scanner (VS120) software by Olympus or confocal microscope Leica Microsystems LSM700 software by Zeiss were used. Sony SH800Z Cell Sorter software was used during acquisition of CaMK2a-Sun1 Fos CUT&RUN data.
Data analysis	For ex vivo electrophysiology, Clampfit 10.6, Axograph (1.7.6) and Graphpad Prism 8 was used. For FFJ snRNA-seq, the Illumina bcl2fastq pipeline was used to generate initial FASTQ files. CellRanger (v3.0.0) pipeline was used to map snRNA-seq and generate count tables data (10x Genomics). Seurat (v3) was used with standard commands (FindVariableFeatures, RunPCA, RunUMAP, FindMarkers) in the R environment for further analysis. For bulk RNA-sequencing and Ribotag sequencing, a custom mapping pipeline (Kim et al., Nature 2010, Burrows-Wheeler Aligner (bwa), RepeatMasker) was used to generate count tables and EdgeR was used to perform differential gene expression analysis. For CUT&RUN, flow cytometry data were analyzed using FlowJo (v10.6). Trimmomatic v0.36, kseq, Bowtie2 v2.2.9, Bedtools v2.27.1, Deeptools v.3.0.2, SEACR v.1.1, and RStudio were used for to identify and analyze peaks. Normalized coverage tracks were visualized using IGV v2.4.10. For in vivo electrophysiology, custom MATLAB scripts were used; Kilosort was used for spike sorting and Phy2 for manual curation. CircStats and Chronux toolboxes were also used in MATLAB. For Morris water maze analysis, custom MATLAB scripts were used for data analysis. Custom code will be made available upon reasonable request.

For manuscripts utilizing custom algorithms or software that are central to the research but not yet described in published literature, software must be made available to editors and reviewers. We strongly encourage code deposition in a community repository (e.g. GitHub). See the Nature Research guidelines for submitting code & software for further information.

Data

Policy information about availability of data

All manuscripts must include a data availability statement. This statement should provide the following information, where applicable:

- Accession codes, unique identifiers, or web links for publicly available datasets
- A list of figures that have associated raw data
- A description of any restrictions on data availability

Ribotag sequencing, FFJ snRNA-seq and CUT&RUN data are deposited into the public repository Gene Expression Ombinus (GEO) with accession number GSE158843. All other data will be shared upon reasonable request.

Field-specific reporting

Please select the one below that is the best fit for your research. If you are not sure, read the appropriate sections before making your selection.

☒ Life sciences ☐ Behavioural & social sciences ☐ Ecological, evolutionary & environmental sciences

For a reference copy of the document with all sections, see nature.com/documents/nr-reporting-summary-flat.pdf

Life sciences study design

All studies must disclose on these points even when the disclosure is negative.

Sample size	No sample-size pre-determination was performed. Sample sizes were chosen based on previously published reports (Xue et al., Nature 2013, Bloodgood et al., Nature 2013, Mardinly et al., Nature 2016, Hrvatin et al., Nature Neuroscience 2018, Harvey et al. Nature 2009).
Data exclusions	Exclusion criteria were pre-established for all datasets. For ex vivo electrophysiology, recordings were discarded if holding current exceeded -500 pA, or if series resistance was greater than 30 MOhms. For dual whole-cell recordings of CA1 pyramidal neurons, recordings were discarded if series resistance differed by more than 30% between the two neurons. For AP-1/FFJ snRNA-seq, nuclei with high mitochondrial content (above 5%) or low gene discovery (below 500 genes) were excluded from further analysis according to standards previously determined to be common practice for single cell studies. The number of cells excluded were similar across all experimental conditions. For bulk and Ribotag RNA-sequencing, and CUT&RUN, no data were excluded. For novel environment snRNA-seq, nuclei with high mitochondrial content (above 5%) or low gene discovery (below 200 genes) were excluded from further analysis. For in vivo electrophysiology, channels that were outside of CA1 were excluded from further analysis. Only well-isolated units were chosen for further analysis. Additionally, single units had to meet the following criteria: detected on fewer than 20 channels, half-max spike width of less than 1 ms, at least 1000 spikes detected in the session, and overall firing rate of > 0.01 spikes per second. Units were divided into putative excitatory and inhibitory subclasses based on the spike trough to peak duration, as described previously (Bartho et al., J Neurophysiol 2004), using a cutoff of 0.7 ms, below which units were labeled as inhibitory interneurons. Due to the low number of inhibitory interneurons recorded, these were excluded from analyses. For Morris water maze behavior tests, mice that did not swim ("floaters") were excluded from further analysis. All data exclusion criteria are described in Methods.
Replication	All attempts at replication were successful by our best efforts. Orthogonal approaches were used to validate each experiment as appropriate. N numbers are provided for every experiment in the figure legends.
Randomization	All samples used were littermates and randomly allocated across experimental conditions.
Blinding	Investigators were not blinded to group allocations during electrophysiological recordings due to the differences in fluorescent labels used to identify pairs of neurons from which to record. Morris water maze experiments were conducted blind to genotype. All analyses were conducted blind to genotype using defined thresholds and criteria. Measurements were made quantitatively with minimal human intervention during data acquisition.

Reporting for specific materials, systems and methods

We require information from authors about some types of materials, experimental systems and methods used in many studies. Here, indicate whether each material, system or method listed is relevant to your study. If you are not sure if a list item applies to your research, read the appropriate section before selecting a response.

Materials & experimental systems

n/a	Involved in the study
☐	☒ Antibodies
☐	☒ Eukaryotic cell lines
☒	☐ Palaeontology and archaeology
☐	☒ Animals and other organisms
☒	☐ Human research participants
☒	☐ Clinical data
☒	☐ Dual use research of concern

Methods

n/a	Involved in the study
☒	☐ ChIP-seq
☐	☒ Flow cytometry
☒	☐ MRI-based neuroimaging

Antibodies

Antibodies used

For histology: Rabbit anti-Fos (Synaptic Systems 226003, Lot 3-28), Mouse anti-Fos (Abcam ab208942, Lot GR3209862-3), Rabbit anti-Npas4 (Lin et al., Nature 2008, APE 5177, Lot 09/09/2004), Rat anti-HA (Sigma ROAHAHA), Rabbit anti-Parvalbumin (Swant, P-27,), Rabbit anti-Fosb (Cell Signaling Technology 2251S, Lot 3, Ref 05/2017), Rabbit anti-Junb (Cell Signaling Technology 3753S, Lot 2, Ref 01/2020), Rabbit anti-cleaved Caspase-3 (Cell Signaling Technology 9661S), and Mouse monoclonal anti-NeuN (Millipore Sigma, MAB377). For Ribotag: Mouse anti-HA (Sigma H3663, Lot 025M4772V). For western blotting: Mouse anti-Myc (DSHB 9E10), Mouse anti-HA (Sigma H3663, Lot 025M4772V), and Rabbit anti-Gapdh (Sigma, G9545). For CUT&RUN: Rabbit anti-Fos (Greenberg lab in-house, affinity eluted #1096), Rabbit IgG (Cell Signaling Technology 2729). Alexa-conjugated secondary antibodies from Life Technologies were used at a 1:250 concentration: Rat Alexa 555 (A21434), Rabbit Alexa 488 (A21206), Rabbit Alexa 555 (A31572), Rabbit Alexa 647 (A31573), Mouse Alexa 555 (A31570), Mouse Alexa 647 (A31571). IRDye-conjugated secondary antibodies from LI-COR were used at a 1:5000 concentration: Mouse IRDye 800CW (926-32210), Rabbit IRDye 800CW (926-32211).

Validation

Rabbit anti-Fos (Synaptic Systems 226003, Lot 3-28), Mouse anti-Fos (Abcam ab208942, Lot GR3209862-3), Rat anti-HA (Sigma ROAHAHA), Rabbit anti-Parvalbumin (Swant, P-27), Rabbit anti-Fosb (Cell Signaling Technology 2251S, Lot 3, Ref 05/2017), Rabbit anti-Junb (Cell Signaling Technology 3753S, Lot 2, Ref 01/2020), Rabbit anti-cleaved Caspase-3 (Cell Signaling Technology 9661S), Mouse monoclonal anti-NeuN (Millipore Sigma, MAB377), Mouse anti-Myc (DSHB 9E10), Mouse anti-HA (Sigma H3663, Lot 025M4772V), Rabbit anti-Gapdh (Sigma, G9545), Rabbit IgG (Cell Signaling Technology 2729), Life Technologies Rat Alexa 555 (A21434), Rabbit Alexa 488 (A21206), Rabbit Alexa 555 (A31572), Rabbit Alexa 647 (A31573), Mouse Alexa 555 (A31570), Mouse Alexa 647 (A31571), Mouse IRDye 800CW (926-32210), and Rabbit IRDye 800CW (926-32211) were validated according to individual datasheets provided by the manufacturers. Rabbit anti-Fos (Greenberg lab in-house, affinity eluted #1096) was validated in the manuscript in the conditional FFJ animals by comparison with a commercial manufacturer-validated Rabbit anti-Fos (Synaptic Systems 226003, Lot 3-28) antibody. Rabbit anti-Npas4 (Lin et al., Nature 2008, APE 5177, 09/09/2004) was previously validated (Lin et al., Nature 2008). Mouse anti-HA (Sigma H3663, Lot 025M4772V) was previously validated (Mardinly et al., Nature 2016).

Eukaryotic cell lines

Policy information about cell lines

Cell line source(s)	293T cells (ATCC).
Authentication	Cell line used was not authenticated. Cell line was used to overexpress proteins of interest.
Mycoplasma contamination	Cell line was not tested for mycoplasma contamination.
Commonly misidentified lines (See ICLAC register)	No commonly misidentified cell lines were used.

Animals and other organisms

Policy information about studies involving animals; ARRIVE guidelines recommended for reporting animal research

Laboratory animals

Animals were handled according to protocols approved by the Harvard University Standing Committee on Animal Care and were in accordance with federal guidelines. The following mouse lines were used: PV-Cre (JAX 017320), CCK-Cre (JAX 012706), PV-Flpo (JAX 022730), C57BL/6J (JAX 000664), Ai14 (JAX 007914), Ai65 (JAX 021875), CaMK2a-Cre (JAX 005359), Rpl22/RiboTag (JAX 029977), Emx1-Cre (JAX 005628), LSL-Sun1-sfGFP-myc (JAX 021039), Dlx5/6-Flpe (Dr. Gord Fishell), Fosfl/fl;Fosbfl/fl;Junbfl/fl (Vierbuchen et al., Molecular Cell 2017), Fos-FlagHA (Vierbuchen et al., Molecular Cell 2017), Npas4-FlagHA (Sharma et al., Neuron 2019), C57BL/6N (Charles River Laboratories; embryonic day 16.5 used for mixed-sex cultured neurons), and Scg2fl/fl (this paper). All animals used were on C57BL6/J or C57BL6/J-mixed background except for embryonic cultured neurons (see above). The ages of the animals used 3-4 weeks for ex vivo electrophysiology, RNA-sequencing, and CUT&RUN, 8-10 weeks for in vivo electrophysiology, and 8-14 weeks for Morris water maze behavioral testing. Mice were housed in ventilated micro-isolator cages in a temperature- and humidity-controlled environment under a standard 12 h light/dark cycle, with food and water provided ad libitum. Both male and female littermate mice were used in similar proportions and divided between control and experimental groups for all experiments conducted. For in vivo silicon probe recordings and Morris water maze experiments, only male littermate mice, housed in a reverse 12 h light/dark cycle, were used.

Wild animals

The study did not involve wild animals.

Field-collected samples	The study did not involve samples collected from the field.
Ethics oversight	Harvard University Standing Committee on Animal Care.

Note that full information on the approval of the study protocol must also be provided in the manuscript.

Flow Cytometry

Plots

Confirm that:

☒ The axis labels state the marker and fluorochrome used (e.g. CD4-FITC).

☒ The axis scales are clearly visible. Include numbers along axes only for bottom left plot of group (a 'group' is an analysis of identical markers).

☒ All plots are contour plots with outliers or pseudocolor plots.

☒ A numerical value for number of cells or percentage (with statistics) is provided.

Methodology

Sample preparation	Hippocampal tissue from CaMK2a-Cre; LSL-Sun1-GFP mice was isolated and dounce homogenized in Buffer HB as described in Methods. Nuclei were isolated from the cell homogenate by layering over 40% and 30% iodixanol (Optiprep), followed by ultracentrifugation and isolation of nuclei at the 30/40% iodixanol interface. Nuclei were diluted 1:1 in CUT&RUN wash buffer supplemented with EDTA, filtered through a 0.35 um strainer, and stained with DRAQ5 at a 1:500 dilution.
Instrument	Nuclei were sorted using a Sony SH800Z Cell Sorter.
Software	Sony SH800Z Cell Sorter software was used during acquisition of data. Data were subsequently analyzed using FlowJo.
Cell population abundance	Singlet DRAQ5-positive nuclei represented roughly 90% of the initial population of sorted material. GFP-positive nuclei gated from the singlet DRAQ5-positive population represented roughly 20% of the initial population of sorted material.
Gating strategy	Unstained nuclei (no DRAQ5) were used to establish the AF700-positive gate for DRAQ5-positive nuclei, and DRAQ5-stained nuclei from wild-type mice (no Sun1-GFP label) were used to establish the GFP-positive gate for Sun1-GFP-positive nuclei. Nuclei stained with DRAQ5 were initially selected based on AF700 signal, followed by selection of nuclei with linearly proportional AF700 area and height signal to isolate singlet nuclei. Sun1-GFP-positive nuclei were then selected from this singlet DRAQ5-positive population using the established GFP-positive gate.

☒ Tick this box to confirm that a figure exemplifying the gating strategy is provided in the Supplementary Information.